NH$_3$ decomposition over Ru/CeO$_2$-PrO$_x$ catalyst under high space velocity conditions for an on-site H$_2$ fueling station

Kiyoshi Yamazaki [a,*], Mitsuru Matsumoto [a], Marie Ishikawa [b], Akinori Sato [b]

[a] *Toyota Central R&D Labs., Inc., Nagakute, Aichi 480–1192, Japan*
[b] *Toyota Motor Corp., Toyota, Aichi 471–8572, Japan*

A R T I C L E   I N F O

A B S T R A C T

From a commercialization perspective, NH$_3$ decomposition catalysts used in on-site H$_2$ fueling stations require a high NH$_3$ conversion of over 99.5%, space velocity (SV) of 30,000 h^{-1} and reaction temperature of 500 °C. To achieve this target, we present Ru catalysts supported on CeO$_2$−PrO$_x$ composites (Ru/CP) prepared by a coprecipitation method. The Ru/CP catalysts exhibited higher activity than the Ru/CeO$_2$ and Ru/PrO$_x$ catalysts and achieved the target with Pr content (=Pr/(Ce+Pr)) of 33−67%. STEM observations and in situ X-ray absorption fine structure analysis revealed that an increase in the Pr content in the catalysts improved the Ru dispersion but inhibited the Ru metalation, owing to a strong "metal–support interaction". Notably, 10% of Ru in the Ru/PrO$_x$ remains an oxide even when reduced at 550 °C. These results suggest that both Ru dispersion and metalation are enhanced at the optimal Pr content, maximizing the number of Ru active sites.

1. Introduction

Global warming, climate change, and energy security issues are motivating the "energy transition" from fossil fuels to renewable energy sources such as solar and wind. The suitable areas of sunshine and wind conditions that allow renewable energy generation are unevenly distributed, and the generated power fluctuates on various time scales. This hinders the production of large amounts of renewable energy. To facilitate the energy transition, new technologies for producing H$_2$ from renewable energy focus on chemically converting H$_2$ into "hydrogen carriers" that can be stored in large quantities for extended periods of time and then reverting them back to H$_2$ when and where it is needed [1–3]. Among the various hydrogen carriers, ammonia is a promising candidate since it readily becomes a liquid suitable for storage under near-ambient conditions [4–8].

On-site NH$_3$-decomposition H$_2$ fueling stations produce highly pure H$_2$ from liquid NH$_3$ feedstock and provide it to proton-exchange membrane (PEM) fuel cell vehicles (FCVs) such as passenger cars, buses, trucks, and forklifts (Fig. 1a) [9]. The development of this type of station could accelerate the spread of PEM-FCVs and steer toward the "energy transition." The station typically has five components: a liquid NH$_3$ storage tank, H$_2$ generator, compressor, accumulator, and dispenser. The H$_2$ generator, which is the core of the station, consists of an NH$_3$

decomposition reactor, an NH$_3$ removal apparatus that removes residual NH$_3$ by the temperature swing technique, and a H$_2$ purification apparatus that separates H$_2$ and N$_2$ by the pressure swing technique (Fig. 1b). Recently, several studies on this type of station have reported that downsizing of the overall equipment to carry out the process in an area comparable to a current gas station, and the H$_2$ production cost necessary to provide fuel cost per mile that is comparable to gasoline are the major issues inhibiting commercialization [10,11].

To address these issues, a microchannel heat-exchanger reactor was developed and utilized for the NH$_3$ decomposition reactor in our previous study [12,13]. This type of reactor allows for downsizing and high thermal efficiency owing to its high surface area to volume ratio [14–16]. The operating temperatures for this reactor were then explored [13]. We set the reaction temperature to 500 °C to (i) reduce the operating energy of the NH$_3$ removal apparatus to maintain the residual NH$_3$ concentration less than 0.1 ppm [17], (ii) avoid excessive heat radiation from the reactor [14,15], and (iii) prevent thermal damage to the reactor [18]. The pretreatment temperature after filling the reactor with the catalyst was adjusted to 550 °C to reduce the cost of the heating device of the reactor and prevent reactor thermal damage. In our preliminary examination, a magnesium oxide-supported ruthenium (Ru/MgO) catalyst, which was reported by Fujitani et al. [19], was applied to the NH$_3$ decomposition catalyst in the reactor. This catalyst exhibited an

---

* Corresponding author.
E-mail address: e0936@mosk.tytlabs.co.jp (K. Yamazaki).

NH_3 conversion of over 99.5% at 500 °C, which is close to the equilibrium conversion, at a space velocity (SV) of 15,000 h^{-1} after pretreatment at 550 °C. By operating the reactor with the Ru/MgO catalyst under these conditions and utilizing the off-gas (low-concentration H_2) released from the H_2 purification apparatus into the NH_3 decomposition reactor, the total energy conversion efficiency of the H_2 generator exceeded 80% [12].

Recently, we performed a cost analysis of H_2 production at on-site NH_3-decomposition H_2 fueling stations and obtained two findings. First, using current technologies such as the Ru/MgO catalyst, the cost of H_2 production exceeded the target for commercialization. Second, it is possible to achieve the target cost when a catalyst performs the same NH_3 conversion at double the SV (see Supplementary material 1.1). Based on this analysis, a "target performance" for the NH_3 decomposition catalyst was set to achieve an NH_3 conversion exceeding 99.5% (residual NH_3 concentration < 2500 ppm) at a reaction temperature of 500 °C and a high SV of 30,000 h^{-1} after pretreatment at 550 °C.

Numerous studies have focused on NH_3 decomposition catalysts and demonstrated that Ru has the highest activity when used as the active species and carbon-based materials, including carbon nanotubes (CNTs), and magnesium oxide (MgO) are effective as supports [7,8,19–45]. Recently, many catalysts containing no precious metals such as Ru have been reported [29,31,33–35,39–41,43,44], but their performance was not close to the above target. Therefore, we chose Ru as the active species. With respect to supports, the C materials (crystal density of approximately 2 g/cm^3) or MgO (crystal density 3.7 g/cm^3) would result in a low bulk density of the catalyst bed. To increase SV, that is, to decrease catalyst bed volume, we focused on the high density supports such as cerium oxide (CeO_2, crystal density 7.2 g/cm^3). If the Ru/CeO_2 catalyst is used to obtain the same NH_3 decomposition activity as a Ru/MgO catalyst of the same weight, the SV would be approximately doubled. Several studies have applied Ru/CeO_2 catalysts to NH_3 decomposition [46–50]. Moreover, lanthanum oxide (La_2O_3), praseodymium oxide (PrO_x (x = 1.5–2.0)), and samarium oxide (Sm_2O_3) which have bulk densities similar to that of CeO_2, have also been used as supports [51–54].

The objective of this study is to develop an NH_3 decomposition catalyst that achieves the "target performance." We investigated the NH_3 decomposition activity of CeO_2, PrO_x, and their composite oxide (CeO_2–PrO_x)-supported Ru catalysts under various conditions of reaction temperatures and SVs.

2. Experimental

2.1. Catalyst preparation

We prepared a series of Ru/CeO_2–PrO_x catalysts by a coprecipitation method. The Ru content of the catalyst was set to 3 wt%. Ruthenium(III) nitrosyl nitrate solution (Ru(NO)(NO$_3$)$_3$, Furuya Metal), cerium(III) nitrate hexahydrate (Ce(NO$_3$)$_3$·6H$_2$O; Fujifilm Wako Chemicals), praseodymium(III) nitrate hexahydrate (Pr(NO$_3$)$_3$·6H$_2$O; Fujifilm Wako Chemicals), and potassium carbonate (K$_2$CO$_3$; Fujifilm Wako Chemicals) were utilized as starting reagents without further purification. A mixed aqueous solution of Ru(NO)(NO$_3$)$_3$, Ce(NO$_3$)$_3$·6H$_2$O, and Pr(NO$_3$)$_3$·6H$_2$O (total volume 200 mL and total metal concentration 1.0 mol/L) and an aqueous solution of K$_2$CO$_3$ (200 mL) were added to deionized water (400 mL) with two fluid pumps (cassette tube pump SMP-23AS, As one) at 10 mL/min, while stirring with a homogenizer (Physcotron NS-57S, Microtec) at 15,000 rpm. The K concentration of the latter solution was set so as the molar ratio K/(Ru*3 + Ce*4 + Pr*3) = 1.0. The resulting precipitate was stirred with the same homogenizer for an additional 15 min at 15,000 rpm, diluted to a total volume of 3 L with deionized water, and then aged at 10–30 °C for 24 h, followed by filtration. As a washing process, the collected solid was dispersed in 3 L of deionized water, stirred with a rotary stirrer at 350 rpm for 30 min, and filtered again. The resulting solid was dried at 110 °C for 20 h, followed by a calcination at 500 °C for 2 h in an air atmosphere. The obtained powder was pressed at 12.3 MPa and ground into pellets of 355–710 μm diameter. The obtained pellet was finally reduced in 20% H$_2$/N$_2$ gas flow at 40 mL/min and 650 °C for 2 h to obtain the pellet-shaped catalyst. Hereinafter, the Ru/CeO_2–PrO_x catalyst having Pr content (molar ratio of Pr/(Ce + Pr)) of xx% is referred to as Ru/CPxx or Ru/CP catalyst, and the catalysts having Pr contents of 0% and 100% are referred to as Ru/CeO_2 and Ru/PrO_x catalysts, respectively. The bulk

(a) Process of on-site NH_3-decomposition H_2 fueling station
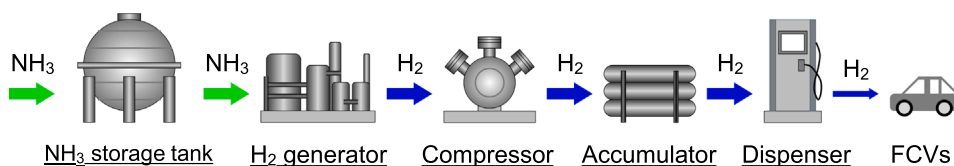
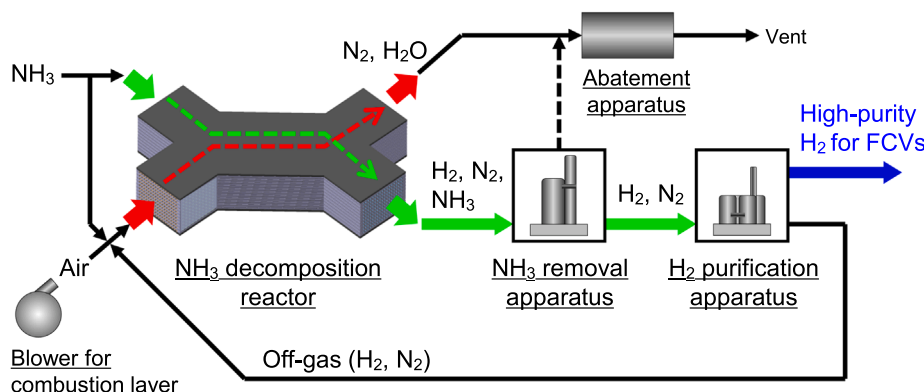## (b) Components of H_2 generator and gas flow

Fig. 1. Schemes of an on-site NH_3-decomposition H_2 fueling station.

density of the obtained pellet catalyst was measured with a graduated cylinder.

As a reference, we chose a Ru/MgO catalyst prepared by a coprecipitation method, which was previously reported by Fujitani et al. [19]. The obtained powdery catalyst was pressed at 12.3 MPa and ground into pellets of 355–710 μm diameter and finally reduced in 20% H_2/N_2 gas flow at 40 mL/min and 650 °C for 2 h.

2.2. Catalyst activity test

We performed catalyst activity tests using an atmospheric fixed-bed, continuous-flow quartz tubular reactor (inner diameter 11.5 mm). The reactor was connected to mass flow controllers at the front, a Fourier-transform infrared (FT-IR) gas analyzer (MultiGas-2030, MKS Instruments) and a gas chromatography (GC) apparatus (GC-2014, Shimadzu) at the rear. To acquire accurate data, the residual NH_3 concentration in the product gas was measured with FT-IR for higher NH_3 conversions (i.e., 95% or higher), while the generated H_2 concentration was measured with GC for lower NH_3 conversions (i.e., less than 95%).

As a typical experimental condition, the reactor contained a catalyst bed consisting of 0.20 g of Ru/CPxx catalyst with quartz wool stoppers at both ends. The catalyst bed was equipped with a thermocouple covered with a quartz tube (outer diameter 2.4 mm) at the center. The volume of the catalyst was 0.20 mL, consisting of a length of 0.20 cm and a cross-sectional area of 1.0 cm^2. As a pretreatment, the catalyst was heated at 550 °C for 1 h under 20% H_2/N_2 gas flow of 40 mL/min. The gas was then exchanged to a flow of 100% NH_3 of 50–300 mL/min at reaction temperatures of 300–500 °C and the outlet gas from the catalyst was measured in steady state.

By controlling the flow rate of 100% NH_3 and the amount of the catalyst, we determined NH_3 decomposition rates at 400–500 °C under the condition that the NH_3 conversion was approximately 8% [19,48]. The required amount of catalyst was mixed with quartz sand of the same pellet size (355–710 μm) and the volume of the catalyst bed was set to 0.20 mL.

2.3. Catalyst durability test

We carried out catalyst durability tests using an atmospheric fixed-bed, continuous-flow quartz tubular reactor (6.0 mm inner diameter), as reported in our previous study [13]. The reactor was connected to mass flow controllers at the front and a FT-IR gas analyzer (Multi-Gas-2030, MKS Instruments) at the rear. The reactor contained a 0.050 g of the catalyst bed, and which was sandwiched both ends with quartz wool. Temperature of the center of catalyst bed was monitored by a thermocouple through a quartz sheath tube (2.4 mm outer diameter).

After a pretreatment at 550 °C, the endurance process at 650 °C and the activity evaluation at 500 °C were repeated. As a pretreatment, the catalyst was heated at 550 °C for 1 h under 20% H_2/N_2 gas flow of 40 mL/min. Then the gas was changed to a 100% NH_3 flow of 25 mL/min, so as SV was adjusted to 30,000 h^{-1}. The catalyst was heated to an endurance temperature of 650 °C and kept for a given period. After the endurance process, the catalyst was cooled to the reaction temperature of 500 °C and the catalytic activity was determined by the residual NH_3 concentration in the product gas with FT-IR. Again, the catalyst was heated to the endurance temperature of 650 °C and kept for a given period. The endurance time corresponds to the total time, that the catalyst was held at the endurance temperature.

2.4. Catalyst characterization

Powder X-ray diffraction (XRD) patterns were measured by using a SmartLab X-ray diffractometer (Rigaku, Cu Kα radiation at 45 kV, 200 mA). The scan range, scan speed, and scan step were 10–90° (2θ), 2°/min, and 0.01°, respectively. By using the Scherrer's equation, we estimated the particle sizes for all phases in the catalysts.

For the measurements of N_2 adsorption/desorption isotherms at the liquid nitrogen temperature (−196 °C), an ASAP 2020 system (Micromeritics) was used. For each measurement, the catalyst was pretreated at 300 °C in vacuo (10^{-5} Torr) for 8 h. The surface areas were calculated with the Brunauer–Emmett–Teller (BET) method. The pore distribution and volume were calculated with the Barrett–Joyner–Halenda (BJH) method.

The CO adsorption amount was estimated with CO pulse adsorption at − 78 °C, by using a fixed-bed reactor (HEMMI Slide Rule, TP-5000). As a pretreatment, the catalysts were reduced for 15 min with 100% H_2 flow at 550 °C, then flushed for 20 min with He flow at the same temperature, then cooled to − 78 °C. Constant volume (0.496 mL) of 60% CO/He pulses were supplied to the sample at − 78 °C. The concentration of passed CO through the reactor outlet was observed using a thermal conductivity detector (TCD). The molar ratio of CO adsorption to Ru content (adsorbed CO/Ru ratio) was estimated from the amount of CO uptake.

The temperature-programmed desorption of CO_2 (CO_2-TPD) measurements were carried out using a fixed-bed reactor (HEMMI Slide Rule, TP-5000). 0.10 g of the catalyst was (i) heated in He gas flow of 20 mL/min at 650 °C for 30 min, (ii) cooled to 50 °C, (iii) fed with 2% CO_2/He gas flow at 20 mL/min for 20 min, and (iv) purged with a 20 mL/min He gas flow at 50 °C for 40 min. The catalyst was finally heated from 50 °C to 650 °C at 10 °C/min in He gas flow of 20 mL/min and the CO_2 concentration in outlet gas was measured using a quadrupole mass spectrometer (Q-mass).

Scanning transmission electron microscopy (STEM) analysis was performed using a HD-2700 (Hitachi High-Tech) equipped with a prove-forming spherical-aberration corrector (Cs-corrector). Secondary Electron (SE) images, bright-field scanning transmission electron microscopy (BF-STEM) images, high-angle annular dark-field scanning transmission electron microscopy (HAADF-STEM) images, and energy dispersive X-ray spectroscopy (EDX) elementary maps were recorded at 200 kV. The catalyst was dispersed in methanol, dropped on a carbon coated copper grid with 2 μm average diameter holes and dried. The average size of Ru particles was analyzed based on the average of over 150 clusters.

In situ X-ray absorption fine structure (XAFS) analysis was conducted by using BL33XU beamline of SPing-8 (Hyogo, Japan) [55]. XAFS data at the Ru, Ce, and Pr K-edge were recorded under transmission mode using a standard Lytle ion chamber. Incident X-ray was monochromatized by a channel-cut Si(111) monochromator for Ru measurements and by a channel-cut Si(220) monochromator for Ce and Pr measurements. For the experimental X-ray adsorption near edge structure (XANES), background subtraction and normalization procedures were conducted using an in-house developed software to obtain the XANES spectrum showing "normalized absorption" as a function of X-ray energy. The value of the X-ray energy at the normalized absorption of 0.5 is referred to as "edge energy" and used as an index of the oxidation state [56]. 120 mg of the catalyst was mixed with 40 mg of Al_2O_3 powder (Nikki-Universal) in an agate mortar, this was pressed into a disk of 10 mm in diameter and loaded into a heating cell. The procedure of analysis was as follows; (i) 5% H_2/He gas flow of 150 mL/min was introduced to the disk-shaped catalyst at 50 °C for 6 min and a XANES spectrum was obtained, (ii) the catalyst was heated from 50 °C to 650 °C at a rate of 20 °C/min while obtaining XANES spectra at 15 s intervals, (iii) the catalyst was maintained at 650 °C for 30 min, then cooled to 50 °C, and a XANES spectrum was obtained. The XANES spectra obtained in (i) – (iii) are referred to as the XANES spectra "before TPR (temperature-programmed reduction)," "during TPR", and "after TPR." Ruthenium metal powder (Ru; Furuya Metal), triruthenium dodecacarbonyl ($Ru_3(CO)_{12}$; Aldrich), tris(acetylacetonato)ruthenium (III) ($Ru(acac)_3$; Furuya Metal), ruthenium chloride dihydrate ($RuCl_3·2H_2O$; Furuya Metal), ruthenium oxide (RuO_2; Furuya Metal), ruthenium oxide hydrate ($RuO_2·2.5H_2O$; Alfa Aesar), and potassium

ruthenate (VI) solution (K_2RuO_4 solution; Furuya Metal, Ru content 4.7 wt%) were used as Ru reference samples. About 20 mg of the Ru reference sample other than the K_2RuO_4 solution was mixed with 80 mg of BN powder (Fujifilm Wako Chemicals) in an agate mortar, pressed into a disk of 10 mm in diameter. The potassium ruthenate (VI) solution was placed in a cell with a thickness of 4.0 mm. The XANES spectra of these Ru reference samples was obtained at 20 °C in air.

3. Results and discussion

3.1. NH₃ decomposition activity

NH₃ decomposition activities of Ru/CeO₂, Ru/CP, Ru/PrOₓ, and Ru/MgO catalysts were compared under various reaction conditions. The bulk density of the Ru/CP catalysts, including Ru/CeO₂ and Ru/PrOₓ catalysts, was approximately 0.97 ± 0.03 g/mL, while that of the Ru/MgO catalyst was 0.46 ± 0.02 g/mL. Under the same SV conditions, the catalyst weight of the Ru/MgO catalyst was about half that of the other catalysts, but by adjusting the Ru content (about 6 wt%), the amount of Ru used in the catalyst bed was the same for all catalysts. Fig. 2a shows NH₃ conversion of the Ru/CeO₂, Ru/CP50, Ru/PrOₓ, and Ru/MgO catalysts at an SV of 30,000 h^{-1} as a function of reaction temperature. The Ru/CP50 catalyst exhibited the highest NH₃ decomposition activity, while the Ru/MgO catalyst was the lowest, regardless of the reaction temperature. Moreover, it was confirmed that even the Ru/CP50 catalyst required a reaction temperature of around 500 °C to achieve an NH₃ conversion over 99.5% (target) or near the equilibrium at an SV of 30,000 h^{-1}. This result indicates that the NH₃ decomposition reactor must be operated at 500 °C or higher.

NH₃ conversion of the Ru/CeO₂, Ru/CP50, Ru/PrOₓ, and Ru/MgO catalysts at 500 °C as a function of SV is shown in Fig. 2b. The NH₃ decomposition activity of the Ru/MgO catalyst was significantly reduced when the SV was increased compared with other catalysts. By contrast, the NH₃ decomposition activity of the Ru/CP50 catalyst remained higher than that of other catalysts under the same high SV conditions. The Ru/CP50 catalyst exhibited an NH₃ conversion over 99.5% (target) at an SV of 30,000 h^{-1}. Since the NH₃ conversion of this catalyst was slightly lower than 99.5% at an SV of 42,000 h^{-1} (99.4%), it is estimated that this catalyst exceeded the NH₃ conversion of 99.5% until about SV of 35,000 h^{-1}.

NH₃ conversion of the Ru/CeO₂, Ru/CP, and Ru/PrOₓ catalysts at 500 °C and an SV of 30,000 h^{-1} as a function of Pr content is shown in Fig. 2c. NH₃ conversions of these catalysts under other conditions as a function of Pr were shown in Figs. S2 and S3. Regardless of the reaction temperature and SV conditions, the NH₃ decomposition activity of the Ru/CP catalysts exhibited a "volcanic trend" with respect to the Pr content and was highest at Pr content of 33–67%. From the above results, it was clarified that the Ru/CP catalyst with Pr content of 33–67% achieved an NH₃ conversion exceeding 99.5% at a reaction temperature of 500 °C and an SV of 30,000 h^{-1} after pretreatment at 550 °C, this was the target performance in this study. On the contrary, the Ru/CeO₂, Ru/PrOₓ, and Ru/MgO catalysts could not achieve this target performance.

3.2. Morphology of supports

Fig. 3a shows XRD patterns of the Ru/CeO₂, Ru/CP, and Ru/PrOₓ catalysts. All observed peaks were attributed to the Ce and Pr compounds, and no peaks due to Ru metal or Ru compounds were detected. This suggests that the crystal particle size of Ru metal or Ru compounds was below the detection limit of the XRD measurement (about 5 nm or less). Peaks attributed to the CeO₂ phase or PrOₓ phase (such as Pr_4O_7, Pr_5O_9, Pr_6O_{11} phases) with the same fluorite-type structure were observed in all catalysts, in addition the hexagonal $Pr(OH)_3$ phase was observed in the Ru/PrOₓ catalyst. Fig. S5 shows XRD patterns of the samples after the calcination at 500 °C, which are the precursors of the Ru/CeO₂, Ru/CP, and Ru/PrOₓ catalysts. A $Pr_2O_2CO_3$ phase was observed along with a Pr_4O_7 phase in the precursor of the Ru/PrOₓ catalyst. It is likely that the $Pr_2O_2CO_3$ phase decomposed into the PrOₓ phase in the reduction at 650 °C and transformed to the $Pr(OH)_3$ phase upon cooling to room temperature and storage in the atmosphere. (The catalyst preparation process in this study consists of three steps: coprecipitation, calcination in air at 500 °C, and reduction (in 20% H_2/N_2 gas flow) at 650 °C).

The lattice constants and the crystal particle sizes of the Ru/CeO₂,
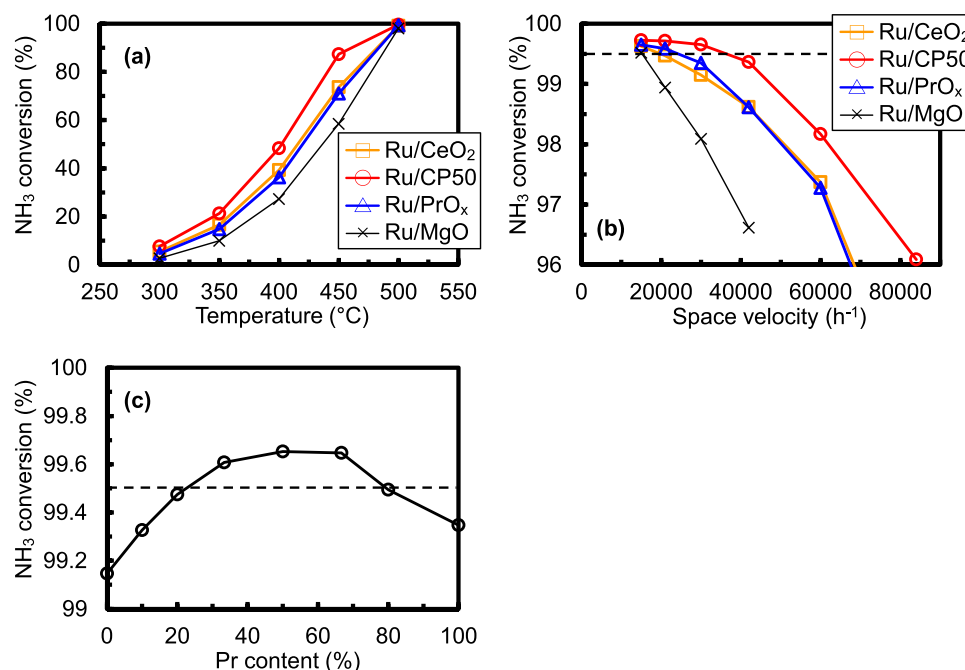
Fig. 2. (a) NH₃ conversion of (□) Ru/CeO₂, (○) Ru/CP50, (△) Ru/PrOₓ and (×) Ru/MgO catalysts at SV of 30,000 h^{-1} as a function of reaction temperature, (b) NH₃ conversion of the above catalysts at 500 °C as a function of SV, and (c) NH₃ conversion at 500 °C and SV of 30,000 h^{-1} as a function of Pr content of Ru/CP catalysts. Black broken lines indicate the target NH₃ conversion (99.5%).
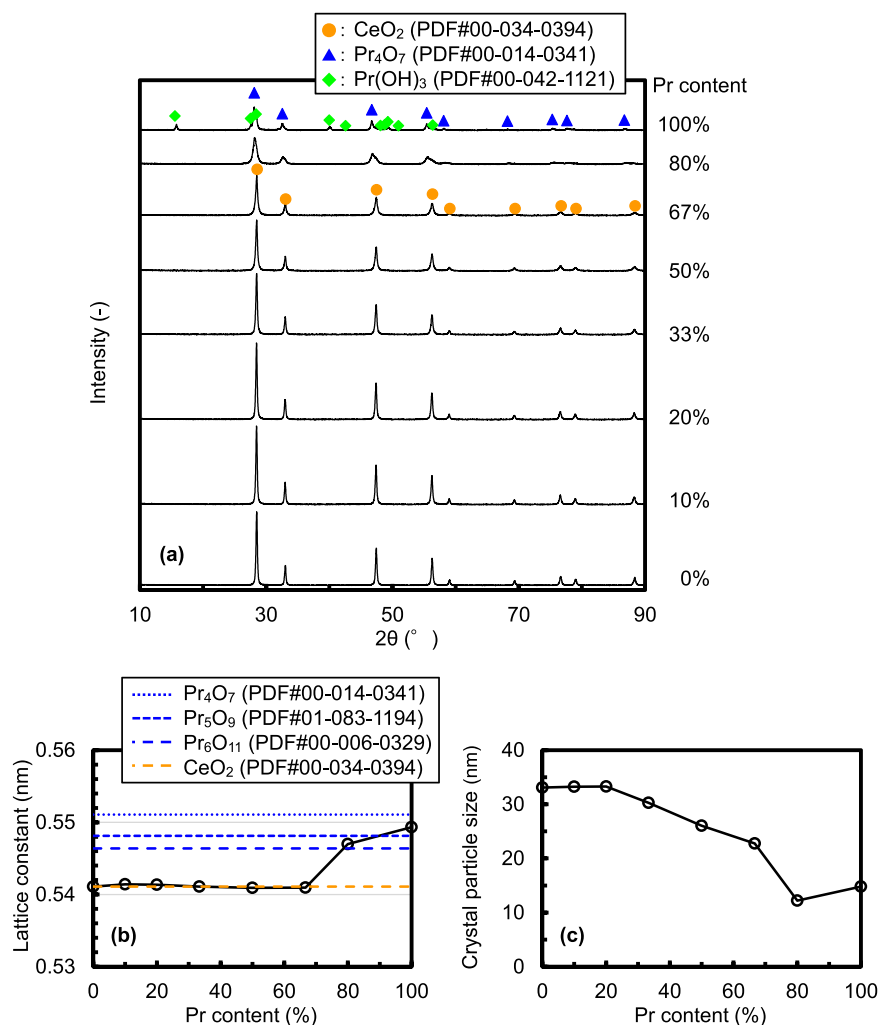
Fig. 3. (a) XRD patterns, (b) lattice constants, and (c) crystal particle sizes of Ru/CeO$_2$, Ru/CP, and Ru/PrO$_x$ catalysts.

Ru/CP, and Ru/PrO$_x$ catalysts calculated from the peaks attributed to the fluorite-type structure are shown in Figs. 3b and 3c. When the Pr content was in the range of 0–67%, the lattice constants of the Ru/CeO$_2$ and Ru/CP catalysts remained almost constant as the Pr content increased, and were almost the same as the values of the CeO$_2$ phase. This suggested that Pr in the supports of these catalysts is tetravalent and has a comparable ionic radius as tetravalent Ce (The effective ionic radii of Ce^{4+}, Pr^{4+}, Ce^{3+}, and Pr^{3+} are 0.097, 0.096, 0.114, and 0.113 nm, respectively [57]). When the Pr content was 80–100%, the lattice constants of the Ru/CP and Ru/PrO$_x$ catalysts increased to values close to those of the Pr$_6$O$_{11}$, Pr$_5$O$_9$, and Pr$_4$O$_7$ phases. This indicated that Pr in the supports of these catalysts existed in a partially reduced state, in

addition to the fact that the Pr(OH)$_3$ phase was generated in the Ru/PrO$_x$ catalyst. The crystal particle size of these catalysts decreased with increasing Pr content and remained almost constant at Pr contents of 80–100%. We assume the crystal growth mechanism as follows; (i) the crystal particle size of Ru and supports in this study are determined during the last reduction step at 650 °C; (ii) The Pr$_2$O$_2$CO$_3$ phase formed after calcination prevents the sintering of the CeO$_2$–PrO$_x$ phase in the last reduction. As the result, the coexistence of Ce and Pr and the inclusion of another Pr$_2$O$_2$CO$_3$ phase suppressed the crystal growth of the fluorite-type CeO$_2$–PrO$_x$ and PrO$_x$ phases.

The specific surface area (SSA) and the pore volume of the Ru/CeO$_2$, Ru/CP, and Ru/PrO$_x$ catalysts are shown in Figs. 4a and 4b. As the Pr
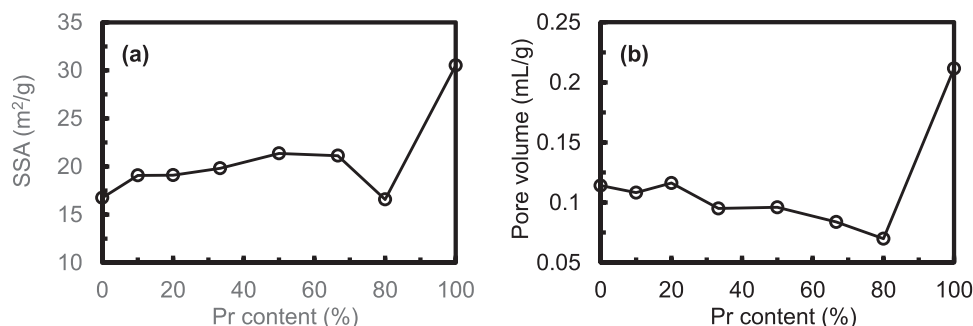

Fig. 4. (a) Specific surface areas (SSA) and (b) pore volumes of Ru/CeO$_2$, Ru/CP, and Ru/PrO$_x$ catalysts.

content increased, the SSA and pore volume gradually increased and decreased, respectively, but at 100% Pr content (Ru/PrO$_x$), both increased significantly. In the Ru/PrO$_x$ catalyst, the formation of multiple crystal phases is the cause of the significantly high SSA and pore volume.

3.3. Morphology of Ru species

To obtain information on the morphology of the Ru species, the CO pulse adsorption method, which generally measures the metal dispersion, was applied to the Ru/CeO$_2$, Ru/CP, and Ru/PrO$_x$ catalysts. Interestingly, as seen in Fig. 5, the adsorbed CO/Ru exhibited a "volcanic trend" with respect to the Pr content and was highest at the Pr content of 33–67%. This trend for Pr content was consistent with that of NH$_3$ decomposition activity. Considering this adsorbed CO/Ru as Ru dispersion, the Ru/CP catalysts with a Pr content of 33–67% had a very high Ru dispersion of about 50%. These results suggested that the main cause of the high activity of these Ru/CP catalysts was the large number of Ru active sites.

The results of STEM analysis on the Ru/CeO$_2$, Ru/CP50, and Ru/PrO$_x$ catalysts are summarized in Figs. 6–8. The SE images of the Ru/CeO$_2$ and the Ru/CP50 catalysts demonstrated small particles supported on large particles (Figs. 6a, 6b, 7a, and 7b). The EDX elementary maps (Figs. S6c, S6d and S7c–S7e), corresponding to Figs. 6a and 7a respectively, showed that the positions of the small particles coincided with those of high Ru content. The high magnification SE images of these catalysts also exhibited small particles supported on large particles (Figs. 6c, 6d, 7c, and 7d). The Ru contents were examined by EDX in the small particle part of the Ru/CeO$_2$ (6−1, 6−3, 6−5) and the Ru/CP50 (7−1, 7−3, 7−5, 7−7, 7−9) catalysts were averaged to 35% and 24%, respectively, and the Ru contents in the large particle part of the Ru/CeO$_2$ (6−2, 6−4, 6−6, 6−7, 6−8) and the Ru/CP50 (7−2, 7−4, 7−6, 7−8, 7−10) catalysts were averaged to 0.77% and 0.58%, respectively. The former Ru contents were much higher than the latter ones. Therefore, the small particles were determined as Ru species (Ru metal or RuO$_2$) in both catalysts. The EDX elementary maps of the Ru/CP50 catalyst showed that the distributions of Ce and Pr were uniform (Figs S7c and S7d). This result indicates that Ce and Pr form a uniformly dispersed solid solution oxide. Then, the large particles in the Ru/CeO$_2$ and Ru/CP50 catalysts were determined to be CeO$_2$ and CeO$_2$–PrO$_x$ solid solutions, respectively. When the size of the Ru particles was measured from these SE images, the average Ru particle sizes of the Ru/CeO$_2$ and Ru/CP50 catalysts were 3.08 nm and 2.29 nm, respectively (Figs. 6e and 7e). It was revealed that the Ru/CP50 catalyst had a smaller Ru particle size than that of the Ru/CeO$_2$ catalyst.

The SE images of the Ru/PrO$_x$ catalyst (Figs. 8a and 8b) also exhibited small particles supported on large particles. However, the number of small particles was decreased and the boundaries between the small and the large particles became unclear compared with the Ru/CeO$_2$ and Ru/CP50 catalysts. The EDX elementary maps (Figs S8c and

S8d) corresponding to the SE image of Fig. S8a show that the position of the small particles coincided with that of high Ru content; however, the high Ru content was not unique to these small particles. The high magnification SE images indicated small particles supported on large particles; however, the boundary between them was obscure (Figs. 8c and 8d). The Ru contents using EDX on small particles (8−1, 8−2, 8−6, 8−10) were averaged and found to be 76% Ru, indicating this small particle is a Ru particle. The "α" region in Fig. 8c appears to be a single crystal of Pr compound (Pr$_5$O$_9$ or Pr(OH)$_3$), because crystal lattice fringes were observed in the corresponding BF-STEM image (Fig. 8e). However, the Ru contents in the "α" region (8−4, 8−5) was 8.2%, which is larger than the overall Ru content in the catalyst. The Ru contents in the parts of large particles where small particles cannot be seen (8−7, 8−9, 8−11, 8−12, 8−13) was found to be 4.4 wt% on average, which is approximately the same as the overall Ru content in the catalyst. Therefore, the Ru species (Ru metal or RuO$_2$) were determined to be present around the particles of the Pr compound near the atomic state or in the monolayer state, as well as in the small particles supported on the large particles of Pr compound. When the small particle size of the Ru species was measured from the SE images, the average Ru particle size of the Ru/PrO$_x$ catalyst was 2.06 nm (Fig. 8 f). In addition, smaller Ru species, not observed as particles, were dispersed on the particles of Pr compound. Therefore, it was revealed that the Ru/PrO$_x$ catalyst had smaller Ru particle size than the Ru/CeO$_2$ and Ru/CP50 catalysts. Notably, the order of Ru particle sizes observed in the STEM analysis: Ru/CeO$_2$ > Ru/CP50 > Ru/PrO$_x$, this was different from the order estimated from the CO pulse adsorption, which had Ru/PrO$_x$ ~ Ru/CeO$_2$ > Ru/CP50.

3.4. Oxidation states of Ru species and supports

The Ru K-edge XANES spectra of the Ru reference samples and the relationship between their valence and the Ru K-edge energy are shown in Figs. 9a and 9b. In Ru$_3$(CO)$_{12}$, C atoms were bonded to Ru atoms, and in RuCl$_3$·nH$_2$O, Cl atoms were bonded to Ru atoms, but in other Ru compounds, O atoms were bonded to Ru atoms. Focusing on Ru metal and Ru compounds in which the O atoms were bonded to Ru atoms, the Ru K-edge energy was found to correlate with the Ru valence very well (Fig. 9b). In agreement with Arčon et al., the shift of the Ru K-edge energy in the XANES spectrum is important information for considering the oxidation state or electronic state of Ru in Ru compounds [58]. This obtained result demonstrated that the Ru K-edge energy corresponds to the oxidation state of Ru species in which O atoms are bonded to Ru atoms.

Comparing the Ru K-edge XANES spectra before and after TPR of the Ru/CP50 catalyst with the spectra of Ru reference samples, the shape of the spectrum before TPR was most similar to a spectrum of RuO$_2$·2.5H$_2$O; however, that after TPR it was closest to the spectrum of Ru metal (Fig. S9b). The change in the Ru K-edge XANES spectra during TPR of the Ru/CP50 catalyst is shown in Fig. 10a. The spectrum gradually changed from a spectrum similar to RuO$_2$·2.5H$_2$O to one similar to Ru metal when heated from 50 °C to 650 °C. As shown by the dotted arrows, some positions of the X-ray did not change during TPR. This suggests that the spectra are composed of the sum of two different spectra, and the proportions of the two are changing. From the above results, it is considered that the Ru species in the Ru/CP50 catalyst primarily existed in RuO$_2$·2.5H$_2$O after catalyst preparation and the changes to the Ru metal when heated under reducing conditions.

The shape of the Ru K-edge XANES spectrum of the Ru/CeO$_2$ catalyst before TPR was between the two spectra of RuO$_2$·2.5H$_2$O and Ru metal, while that of the Ru/PrO$_x$ catalyst was most comparable to the spectrum of RuO$_2$·2.5H$_2$O (Figs S9a and S9c). The Ru K-edge XANES spectra after TPR of the Ru/CeO$_2$ and Ru/PrO$_x$ catalysts were most like that of Ru metal. The change in the Ru K-edge XANES spectra during TPR of the Ru/CeO$_2$ and the Ru/PrO$_x$ catalysts indicated that the Ru species in the form of RuO$_2$·2.5H$_2$O was reduced to the form of Ru metal in both
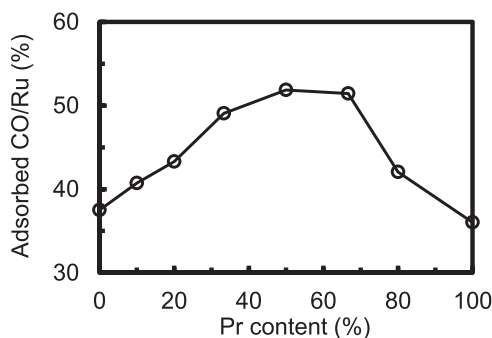

Fig. 5. Molar ratio of CO adsorption amount to Ru content (adsorbed CO/Ru) of Ru/CP catalysts as a function of Pr content.
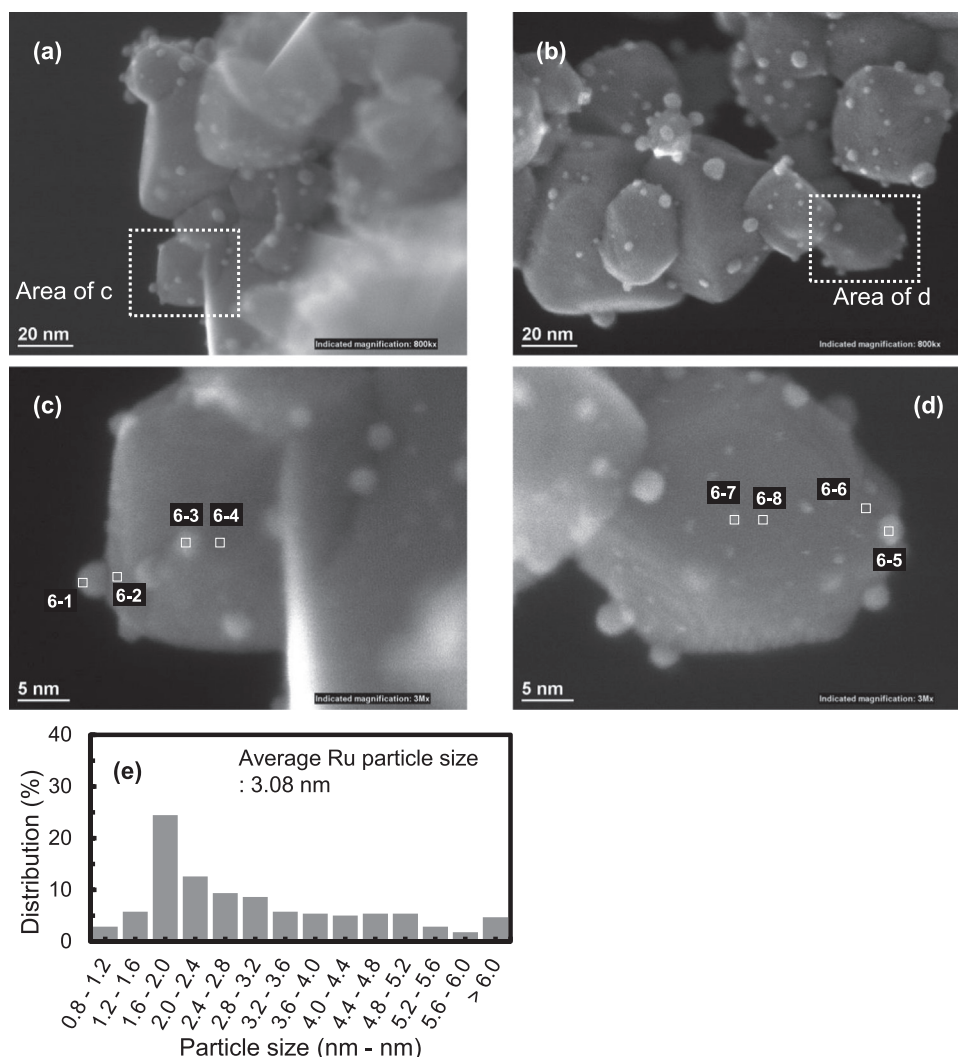
Fig. 6. (a, b) SE images, (c, d) high magnification SE images, and (e) the size distribution of Ru particles of Ru/CeO$_2$ catalyst.

catalysts.

Fig. 10b shows changes in the Ru K-edge energy of the Ru/CeO$_2$, Ru/CP50, and Ru/PrO$_x$ catalysts as a function of catalyst temperature during TPR. This indicated that about half of the Ru species in the Ru/CeO$_2$ catalyst was in the oxide state, the rest was in the metal state, and the Ru species in the Ru/CP50 and Ru/PrO$_x$ catalysts were primarily oxide before TPR (after catalyst preparation). In the catalyst preparation process, the Ru species in these catalysts were reduced to an Ru metal state in 20% H$_2$/N$_2$ gas flow at 650 °C for 2 h, therefore, it was revealed that majority of the Ru species changed to an oxide state when stored in the air at room temperature after catalyst preparation. The Ru species in the Ru/CeO$_2$, Ru/CP50, and Ru/PrO$_x$ catalysts started to be reduced from the oxide state around 130 °C, 200 °C, and 240 °C, respectively, and then rapidly reduced around 150 °C, 240 °C, and 280 °C, respectively, and were gradually reduced to the metal state. The temperature at which the Ru species is reduced from the oxide to the metal state is in the order of Ru/CeO$_2$ < Ru/CP50 < Ru/PrO$_x$, with higher Pr contents, requiring higher temperatures for the Ru species to be reduced. Interestingly, the Ru species in the Ru/CeO$_2$ and Ru/CP50 catalysts were predominantly in the metal state around 550 °C; however, approximately 10% of the Ru species in the Ru/PrO$_x$ catalyst remained in the oxide state even when reduced at 550 °C. These results strongly suggest that approximately 10% of the Ru species in the Ru/PrO$_x$ catalyst were not measured in the CO pulse adsorption and did not function as active sites for NH$_3$ decomposition in the catalyst activity test after pretreatment at 550 °C.

Comparing the Ce K-edge XANES spectra before and after TPR of the Ru/CeO$_2$ and Ru/CP50 catalysts with the spectra of Ce reference samples, the shapes of the spectra of both catalysts before and after TPR were similar to that of the spectrum of CeO$_2$ (Figs. S10a and S10b). Comparing the Pr K-edge XANES spectra before and after TPR of the Ru/CP50 and the Ru/PrO$_x$ catalysts with the spectra of Pr reference samples, the shapes of the spectra before TPR of both catalysts were comparable to that of the spectrum of Pr$_6$O$_{11}$, and the shapes of the spectra after TPR of both catalysts appeared to roughly imitate the spectra of Pr$_6$O$_{11}$ and Pr$_2$(CO$_3$)$_3$·8H$_2$O (Figs. S10c and S10d).

Fig. 11a shows changes in the Ce K-edge energy of the Ru/CeO$_2$ and the Ru/CP50 catalysts as a function of catalyst temperature during TPR, together with the values of the Ce reference samples. Since the Ce K-edge energy corresponds to the oxidation state of Ce as in the case of Ru, it is considered that Ce in both catalysts was primarily tetravalent after preparation (before TPR), but was gradually reduced, and approximately 15% of Ce became trivalent at 650 °C. Fig. 11b shows changes in the Pr K-edge energy of the Ru/CP50 and the Ru/PrO$_x$ catalysts as a function of catalyst temperature during TPR, together with the values of the Pr reference samples. Approximately 90% in the Ru/CP50 and 50% in the Ru/PrO$_x$ catalysts were tetravalent after preparation (before TPR). These results agree with the results deduced from the lattice constants from the XRD measurements (Fig. 3b). The Pr in the Ru/CP50 and Ru/PrO$_x$ catalysts began to be reduced around 150 °C and 200 °C,
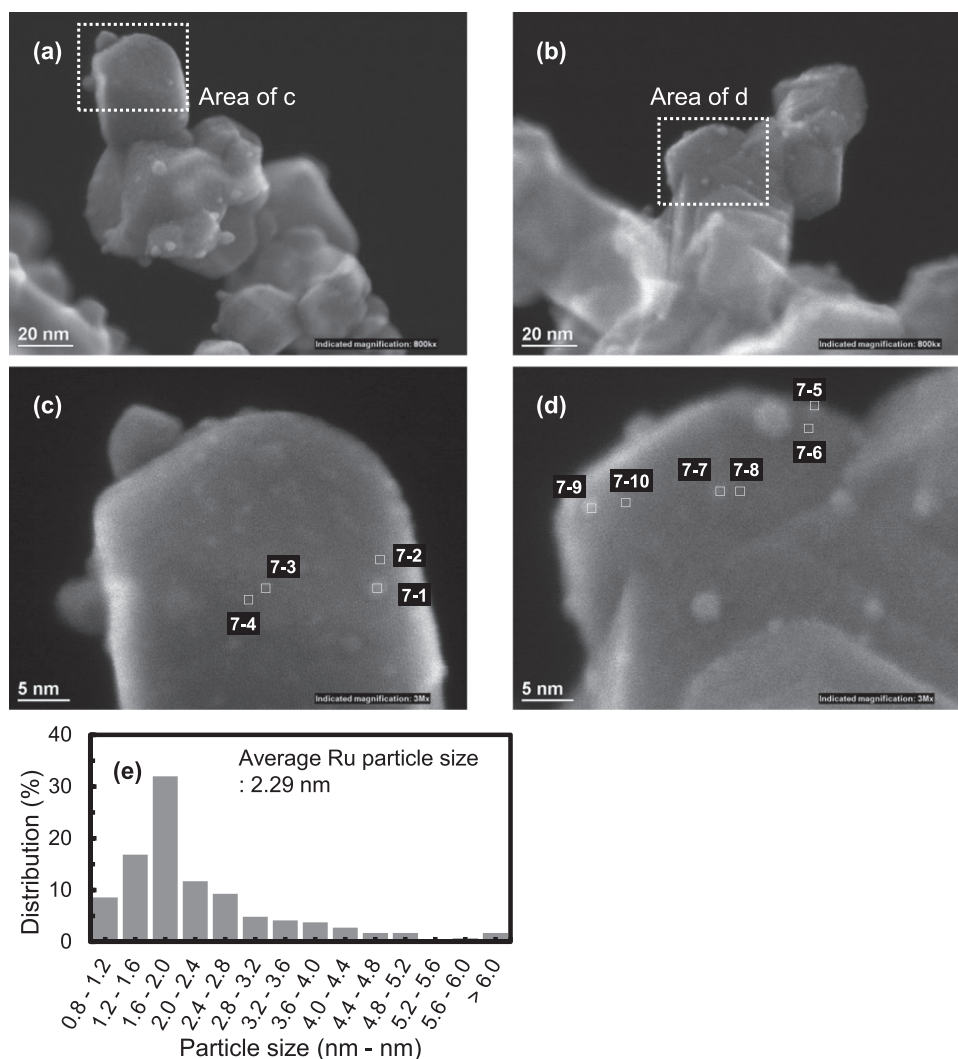
Fig. 7. (a, b) SE images, (c, d) high magnification SE images, and (e) the size distribution of Ru particles of Ru/CP50 catalyst.

respectively, then are rapidly reduced around 200 °C and 240 °C, respectively, and become predominantly trivalent over 240 °C and 280 °C, respectively. Ru/PrOₓ reduced at a higher temperature than Ru/CP50, and the lower the Pr content (the higher the Ce content), the easier Pr was reduced. When Pr becomes trivalent in the PrOₓ crystal, the Pr ionic radius becomes larger and the crystal lattice is distorted, so it is expected that it becomes harder to reduce Pr. The presence of tetravalent Ce with a small ionic radius in the CeO_2–PrO_x solid solution would alleviate the distortion of the crystal lattice, and consequently facilitate the reduction of Pr in the Ru/CP catalysts.

In comparison with the K-edge energies of Ru, Ce, and Pr during TPR in Figs. 10b, 11a, and 11b, no linkage between the Ru reduction and the Ce reduction was observed in the Ru/CeO₂ and Ru/CP50 catalysts. On the contrary, the Ru reduction followed the same trend as the Pr reduction at a temperature approximately 40 °C higher in the Ru/CP50 and the Ru/PrOₓ catalysts. This linkage indicates a strong interaction between Ru and PrOₓ in the supports (namely, metal–support interaction), where the support transports oxygen from the PrOₓ to the Ru through a "Ru–O–Pr bond". The Ru/PrOₓ catalyst is considered to have more Ru–O–Pr bonds than the Ru/CP50 catalyst. The Ru and Pr reductions in the Ru/PrOₓ catalyst occurred at temperatures 40–50 °C higher than those in the Ru/CP50 catalyst. The Ru/PrOₓ catalyst has oxidized Ru species even at 650 °C. These results strongly suggest that the Ru/CP catalysts with the higher Pr content have the stronger metal–support interaction.

3.5. NH₃ decomposition kinetics

Based on the results of the morphology and the oxidation state of the Ru species, the CO adsorption measured by CO pulse adsorption was regarded as the number of Ru active sites, which works after pretreatment at 550 °C. Then, a kinetic analysis of NH₃ decomposition was carried out to obtain the NH₃ decomposition rate per unit catalyst mass, turnover frequency (TOF), and apparent activation energies (Eₐ). NH₃ decomposition rate of the Ru/CeO₂, Ru/CP, Ru/PrOₓ, and Ru/MgO catalysts at reaction temperatures of 500 °C as a function of Pr content is shown in Fig. 12a. NH₃ decomposition rates of these catalysts at reaction temperatures of 400 °C, 425 °C, 450 °C, and 475 °C are shown in Figs. S11a–S11d. The NH₃ decomposition rate of the Ru/CP catalysts exhibited a "volcanic trend" with respect to the Pr content and was at its highest at the Pr content of 33–67%, regardless of the reaction temperature.

TOFs of the Ru/CeO₂, Ru/CP, Ru/PrOₓ, and Ru/MgO catalysts at reaction temperatures of 500 °C as a function of Pr content are shown in Fig. 12b. TOFs of these catalysts at reaction temperatures of 400 °C, 425 °C, 450 °C, and 475 °C are shown in Figs. S12a–S12d. At each reaction temperature, the TOF of the Ru/CP catalysts was almost constant regardless of the Pr content. This result indicates that the NH₃ decomposition rate per Ru active site does not change for all the Ru/CP catalysts, and the main factor determining the NH₃ decomposition activity was the number of active sites. Surprisingly, the Ru/PrOₓ catalyst had a
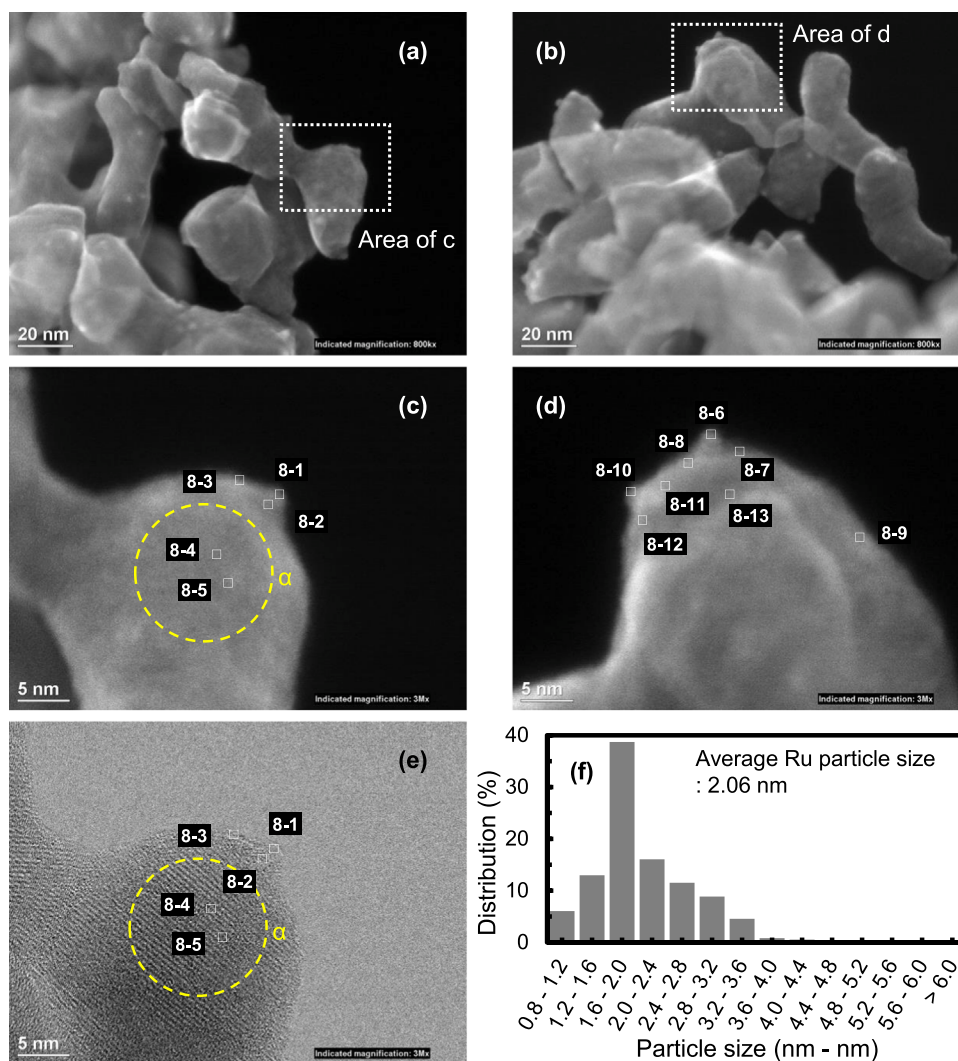
Fig. 8. (a, b) SE images, (c, d) high magnification SE images, (e) BF-STEM image of the same area as image c, and (f) the size distribution of Ru particles of Ru/PrOₓ catalyst.
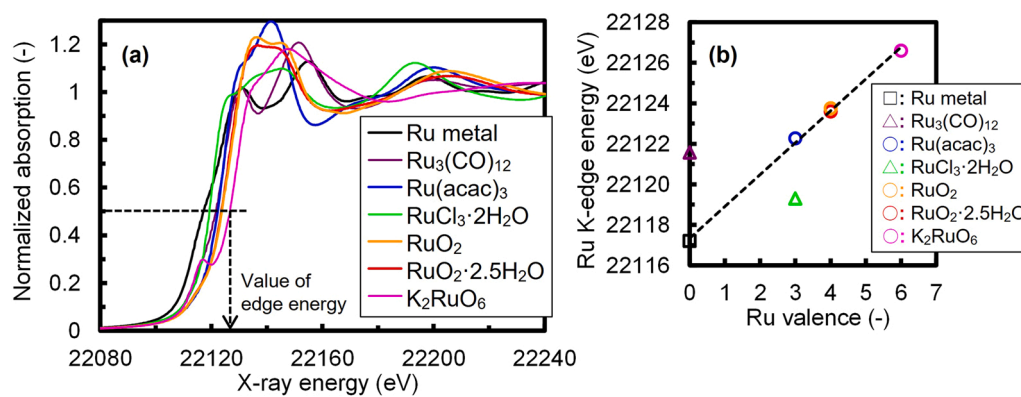
Fig. 9. (a) Ru K-edge XANES spectra of Ru reference samples and (b) relationship between Ru valence and Ru K-edge energy of Ru reference samples; (□) Ru metal, (△) $Ru_3(CO)_{12}$, (○) $Ru(acac)_3$, (△) $RuCl_3 \cdot 2H_2O$, (○) RuO_2, (○) $RuO_2 \cdot 2.5H_2O$, and (○) K_2RuO_6.

TOF about 19% higher than the other catalysts. This could be related to the PrOₓ support with smaller crystal particle size, larger SSA and larger pore volume, compared with those of other CeO_2 and CeO_2–PrOₓ supports (Figs. 3c, 4a and 4b), generally such supports are advantageous for catalytic activity [13].

Fig. 12c shows Arrhenius plots for the NH_3 decomposition rate over
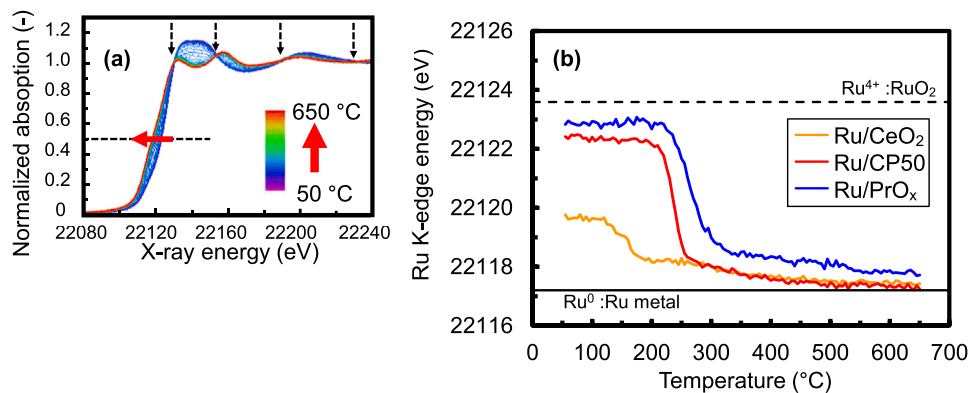
Fig. 10. (a) Change in the Ru K-edge XANES spectrum of Ru/CP50 catalyst during TPR, and (b) changes in the Ru K-edge energy of Ru/CeO$_2$, Ru/CP50, and Ru/PrO$_x$ catalysts during TPR; Black full and broken lines indicate Ru K-edge energy of Ru metal and RuO$_2$ reference samples, respectively.
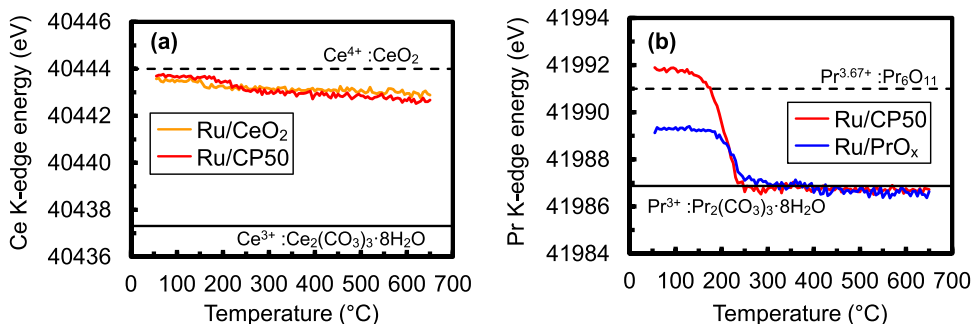

Fig. 11. (a) Changes in Ce K-edge energy of Ru/CeO$_2$ and Ru/CP50 catalysts during TPR; Black full and broken lines indicate Ce K-edge energy of Ce$_2$(CO$_3$)$_3$·8H$_2$O and CeO$_2$ reference samples, respectively. (b) Changes in Pr K-edge energy of Ru/CP50, and Ru/PrO$_x$ catalysts during TPR; Black full and broken lines indicate Pr K-edge energy of Pr$_2$(CO$_3$)$_3$·8H$_2$O and Pr$_6$O$_{11}$ reference samples, respectively.
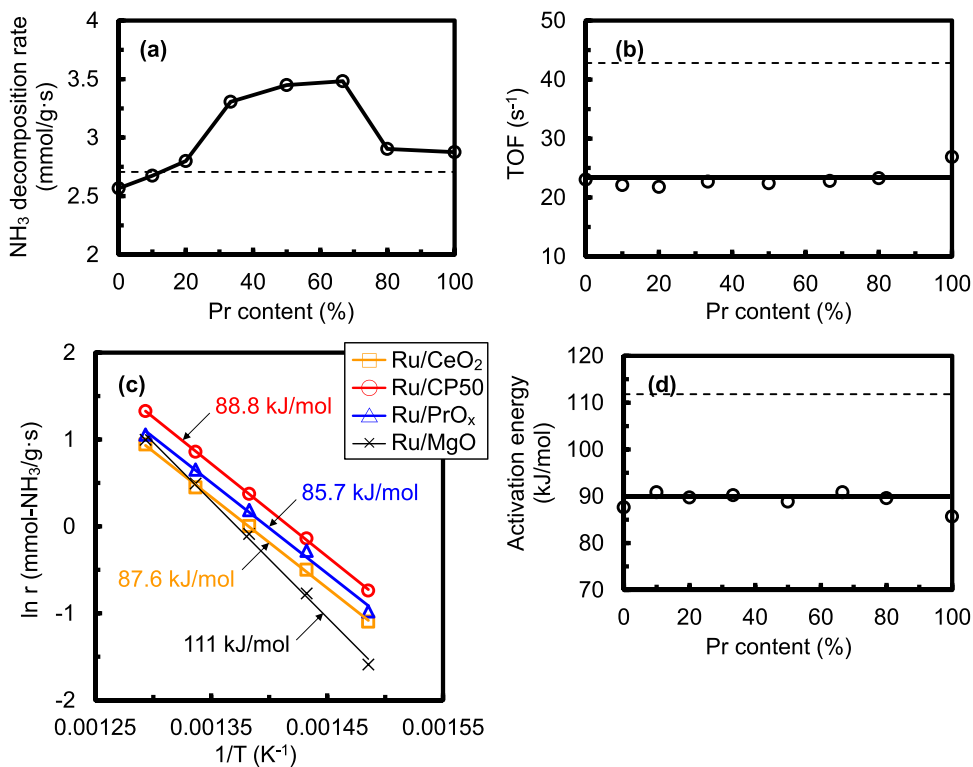
Fig. 12. (a) NH$_3$ decomposition rate at 500 °C as a function of Pr content in the Ru/CP catalysts, (b) TOF at 500 °C calculated assuming that the CO adsorption amount equates to the number of Ru active sites, (c) Arrhenius plots of NH$_3$ decomposition rates, and (d) activation energy as a function of Pr content in the Ru/CP catalysts. Black broken lines indicate the values of the Ru/MgO catalyst.

the Ru/CeO$_2$, Ru/CP50, Ru/PrO$_x$, and Ru/MgO catalysts. A strong linear relationship was observed with any catalyst in the reaction temperature range of 400–500 °C (correlation coefficient (R^2) > 0.995). Similar linear relationships were obtained with the other Ru/CP catalysts. The E$_a$ of these catalysts as a function of Pr content are shown in Fig. 12d. The E$_a$ of the Ru/CP catalysts was almost constant regardless of the Pr content. This result indicates that the properties of Ru active sites of Ru/CeO$_2$ and Ru/CP catalysts were almost the same. Only the Ru/PrO$_x$ catalyst had an E$_a$ of approximately 4 kJ/mol (4%) smaller than the other catalysts. This could be related to the PrO$_x$ support which had smaller crystal particle size, larger SSA, and larger pore volume (Figs. 3c, 4a and 4b) for the same reasons as above.

Several studies have reported correlations between Ru particle size and NH$_3$ decomposition activity for supported Ru catalysts. These studies found a trend that the TOF increased with Ru particle size in the wider range (approximately 0.8–8 nm) [8,59–61], compared to our study (2.06–3.08 nm). Karim et al. exhibited that the TOF increased gradually with Ru particle size from 0.8 nm to 4.4 nm, then sharply above 4.4 nm in their Ru/γ-Al$_2$O$_3$ catalysts [60]. It should be noted that the TOF is often calculated from the number of active sites determined from the Ru particle size in TEM observations in these reports. On the other hand, we took more essential approach; the number of Ru active sites (which works after pretreatment at 550 °C) were evaluated from CO adsorption mounts. We found the number of active sites were decreased when the particle size was small in the Ru/PrO$_x$ catalyst. As the result the TOF was independent to the Ru particle size. We consider the absence of Ru particle size effect is caused by the the narrow range of Ru particle size and the estimation method of the number of Ru active sites.

When comparing the NH$_3$ decomposition rate per unit catalyst mass of the Ru/CP catalysts with that of the Ru/MgO catalyst, the SV of the Ru/CP catalysts was about twice that of the Ru/MgO catalyst due to the difference in bulk density of the catalysts, as described above. Even when compared by weight, the NH$_3$ decomposition rate of the Ru/CP catalysts with a Pr content of 33–67% was higher than that of the Ru/MgO catalyst (Fig. 12a) and the advantage of the Ru/CP catalysts over the Ru/MgO catalyst was larger as the reaction temperature decreased (Figs. S11a–S11e). On the contrary, the TOF of the Ru/MgO catalyst was higher than the Ru/CP catalysts (Fig. 12b and S12a–S12e). This result indicates that the lower NH$_3$ decomposition activity of the Ru/MgO catalyst was due to a much lower number of active sites (adsorbed CO/Ru = 12%), compared with those of the Ru/CP catalysts (Fig. 5). The E$_a$ of the Ru/MgO catalyst was higher than the Ru/CP catalysts. As also shown in Figs. S11a–S11e, this result indicates that the Ru/MgO catalyst became less active at low temperatures than the Ru/CP catalysts.

3.6. Mechanism of high NH$_3$ decomposition activity of Ru/CeO$_2$–PrO$_x$ catalyst

As shown by STEM analysis (such as Figs. 6e, 7e, and 8f in Section 3.3), this study confirmed that the Ru particle size decreased with increasing the Pr content in the Ru/CP catalysts, including the Ru/CeO$_2$ and Ru/PrO$_x$ catalysts, after catalyst preparation process. It is generally known that "metal–support interaction" in supported metal catalysts inhibits metal particle growth (sintering) through "metal–O–M (where M is the cation in the support) bonds", such as the Pt–O–Ce bonds in the Pt/CeO$_2$ catalyst [62]. The "Ru–O–M (where M is the Pr or Ce cation) bonds" are first formed in the coprecipitation and then calcinated in air at 500 °C, under oxidizing conditions. At this stage, Ce exists mainly in the tetravalent state and Pr exists in the trivalent and tetravalent states, as shown by CeO$_2$, Pr$_4$O$_7$, and Pr$_2$O$_2$CO$_3$ phases in Fig. S5. To investigate the metal–support interaction, CO$_2$-TPD was measured for the samples after the calcination at 500 °C, which are the precursors of the Ru/CP catalysts (Fig. 13). The higher the Pr content, the higher the temperature at which peak CO$_2$ desorption occurred and the temperature at which CO$_2$ desorption was completed. This result indicates that the increased
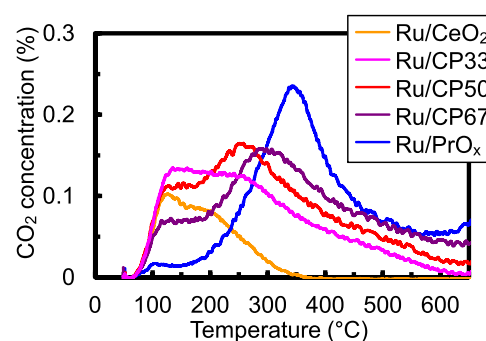

Fig. 13. CO$_2$-TPD profiles for precursors of Ru/CP catalysts, which are samples after coprecipitation and calcination in air at 500 °C in catalyst preparation process.

Pr content enhanced the basicity of the supports. Although Ce and Pr have similar electronegativities, trivalent Pr cation is less electronegative than tetravalent Ce cation [63]. This would be the main reason why the PrO$_x$ in the support has a higher basicity than the CeO$_2$ in the supports. Several studies have demonstrated that high basicity is accompanied by strong metal–support interactions, which is typically investigated by CO$_2$-TPD and H$_2$-TPR analyses [64–66]. Just as the oxygen in highly basic metal oxides binds strongly to protons, the oxygen in the support PrO$_x$ is likely to bind strongly to the cationic ruthenium (Ru$^{δ+}$). Therefore, it is considered that the PrO$_x$ in the supports has the stronger metal–support interaction than the CeO$_2$ in the supports and inhibits Ru particle growth through the Ru–O–Pr bonds during the last reduction at 650 °C. This is also supported by the results of in situ XAFS analysis (Fig. 10b in Section 3.4). This strong metal–support interaction is mainly responsible for the decrease in the Ru particle size with increasing the Pr content in the Ru/CP catalysts after preparation process. The smaller Ru particle size was assumed to lead to the larger number of Ru active sites.

In contrast, as shown by in situ XAFS analysis (such as Fig. 10b), this study revealed that the increased Pr content in the Ru/CP catalysts inhibited the reduction of Ru species from the oxide to the metal state. This is believed to be also due to the same strong metal–support interaction. Surprisingly, nearly 10% of the Ru species in the Ru/PrO$_x$ catalyst remained in the oxide state even when reduced at 650 °C. Generally, only the Ru species in the metal state can function as Ru active sites. Therefore, the excessively strong metal–support interaction can reduce the number of Ru active sites in the Ru/CP catalysts.

As shown by kinetic analysis (such as Figs. 12b and 12d in Section 3.5), this study demonstrated that the properties of the Ru active sites, represented by the turnover frequency(TOF) and the apparent activation energy (E$_a$), are very similar regardless of the Pr content in the Ru/CP catalysts after preparation process. Figs. 11a and 11b showed that most of Pr in the Ru/CP50 and Ru/PrO$_x$ catalysts is trivalent and approximately 15% of Ce in the Ru/CeO$_2$ and Ru/CP50 catalysts is trivalent under reducing conditions around 500 °C, which is close to NH$_3$ decomposition conditions. Suda et al. estimated an oxygen storage/release capacity from CeO$_2$ per unit surface area (0.85 μmol-O$_2$/(m^2/g)) at 500 °C [67]. The SSA of the Ru/CeO$_2$ and Ru/CP50 catalysts were 17 and 21 m^2/g, respectively (Fig. 4a). Assuming that Ce is reduced and O$_2$ is released only from the surface of these catalysts, 1.0% and 1.3% of Ce changes from tetravalent to trivalent, respectively, which are much less than the observed 15%. Since the surface Ce can be reduced before the bulk species done, the reduction of the surface Ce is believed to be completed under NH$_3$ decomposition conditions. Ce and Pr cations have close ionic radius [57] and identical fluorite-type crystal structure, both have similar electronegativities at same oxidation states. Therefore, regardless of the Pr content, the surface of the CeO$_2$–PrO$_x$ support is considered to generate approximately the same amount of oxygen vacancies and donate electrons to the Ru active sites to the same degree

[63]. This is the main reason why the properties of the Ru active sites (TOFs and E_a) are very similar in the Ru/CP catalysts after the preparation process.

From the above results, a mechanism for the high activity of the Ru/CP catalysts is suggested in Fig. 14. That is, the NH_3 decomposition activity of the Ru/CP catalysts is determined by the number of Ru active sites, which is determined by both the Ru particle size (Ru dispersion) and the ease of the reduction of Ru species from the oxide to the metal state (Ru metalation). The activity exhibits a volcanic trend with respect to the Pr content, as the optimum metal–support interaction enhanced both the Ru dispersion and the Ru metalation to maximize the number of Ru active sites. It should be noted that CO pulse adsorption was found to be an effective method for measuring the number of Ru active sites for the Ru/CP catalysts, because it can detect the Ru sites exposed in the metallic state in an atmosphere close to the operating conditions.

It is well known that the catalyst preparation process has strong influence on the activity of supported metal catalysts. We have examined the effects from (a) residual potassium (K) and (b) precipitation method, as follows.

A series of Ru/CeO$_2$–PrO$_x$ catalysts examined in this study contain a small amount of K due to the use of K_2CO_3 as a precipitant in the coprecipitation method. According to EDX analysis, the K contents of the Ru/CeO$_2$, Ru/CP50 and Ru/PrO$_x$ catalysts were 0.23, 0.14 and 0.13 wt %, respectively, with corresponding K/Ru molar ratios of 0.20, 0.12. and 0.11. Several studies have reported the effect of K content on supported Ru catalysts. Ju et al. reported that K-modified Ru/MgO catalyst with K/Ru of 0.5 showed higher activity than that with K/Ru of 1.0 [28]. Wang et al. reported that K-modified Ru/CNTs catalyst exhibited the maximum promoting effect at a K/Ru molar ratio of 2.0 [21]. Compared to the catalysts in these reports, the Ru/CeO$_2$–PrO$_x$ catalysts in this study contain much lower K content. As a preliminary study, we investigated the effect of precipitants used in the coprecipitation method. Four Ru/CeO$_2$–PrO$_x$ catalysts with Pr content of 50% were prepared using K_2CO_3, $(NH_4)_2CO_3$, KOH, and NH_3 solutions as precipitants. The order of precipitants in NH_3 decomposition activity was $K_2CO_3 > (NH_4)_2CO_3 >> NH_3 > KOH$ (Fig. S4). This order agrees very well with the the order of adsorbed CO/Ru; K_2CO_3 (52%) > $(NH_4)_2CO_3$ (36%) >> NH_3 (0.39%) > KOH (0.13%). These results indicate that K_2CO_3 is the most effective precipitant to improve Ru dispersion corresponding to the number of Ru active sites. To clarify the effect of K on Ru, the catalyst prepared with $(NH_4)_2CO_3$ was modified with K using KNO_3 solution with K/Ru molar ratios of 0.15. The activity of the obtained K-modified catalyst was almost the same as that of the original catalyst (Fig. S4). From the above results, we conclude that the effect of K on promoting the activity of Ru in the Ru/CeO$_2$–PrO$_x$ catalysts is minor in this study, mostly because the K content is small.

It is worthwhile to mention that the catalyst preparation method also has effects on the number of Ru active sites. Kikugawa et al. recently reported a strong interaction between Ru and CeO$_2$–PrO$_x$ supports in their Ru/CeO$_2$–PrO$_x$ catalysts for an NH_3 synthesis reaction [68]. They prepared the catalysts with an Ru content of 1 wt% by the impregnation method using Ru solutions and CeO$_2$–PrO$_x$ supports. The CO adsorption amounts (adsorbed CO/Ru), or the Ru dispersion, of these catalysts were somewhat smaller than those of this study (Fig. 5, approximately 50%). The Ru dispersion became lower as its loading increased in general, but we found opposite results in this study. We hypothesize that the coprecipitation method used in this study improved the Ru dispersion compared to impregnation method, because the coprecipitation method could form fine particles of Ru and supports, which contributed to the formation of Ru active sites.

3.7. Comparison of catalytic activity over various catalysts

In order to compare the catalytic activity obtained in this study with those reported in the review literature [22,36–38], the NH_3 decomposition rates (per catalyst mass) and TOF values are shown in Table 1. When compared at a reaction temperature of 450 °C, Hu et al. reported an NH_3 decomposition rate of 1.10 mmol/g$_{cat}$·s for Ru/CeO$_2$ [48], while Le et al. reported 0.29 mmol/g$_{cat}$·s for Ru/La$_{0.33}$Ce$_{0.67}$O$_x$ [49], and Ju et al. reported 0.39 and 0.30 mmol/g$_{cat}$·s for K–Ru/MgO and Ru/MgO, respectively [28,30]. The NH_3 decomposition rate obtained in this study for the Ru/CP50 catalyst was 1.45 mmol/g$_{cat}$·s, which was the highest value of any catalyst reported in the literature so far. When compared at a reaction temperature of 400 °C, Yin et al. reported a NH_3 decomposition rate of 0.59 mmol/g$_{cat}$·s for K–Ru/MgO–CNTs [23], while Fujitani et al. reported 0.29 mmol/g$_{cat}$·s for Ru/MgO [19]. The NH_3 decomposition rate obtained in this study for the Ru/CP50 catalyst was 0.48 mmol/g$_{cat}$·s, which is in the range reported for the most active catalysts. However, when molded into pellet catalysts, the bulk densities of the CNTs- and MgO-supported catalysts were approximately 10–15% and 50% of the CeO$_2$-supported catalyst, respectively. Therefore, the Ru/CP50 catalyst could show a higher NH_3 decomposition rate (per catalyst volume) than the K–Ru/MgO–CNTs and the Ru/MgO catalysts under the same SV conditions. Therefore, the Ru/CP catalysts exhibited the highest level of NH_3 decomposition activity, per catalyst volume, among any catalyst reported in the literature so far and as such, could be the most effective for application in H$_2$ fueling stations.

3.8. Durability of Ru/CeO$_2$–PrO$_x$ catalyst

In the cost analysis, the effective life of the reactor needs to be approximately 80,000 h (for example, 12 years at 75% operation rate) from the viewpoint of commercialization. Our preliminary study on the temperature distribution in a microchannel heat-exchange reactor demonstrated that the temperature could reach > 570 °C, when the reactor was maintained at 500 °C [12]. Therefore, the catalyst needs to
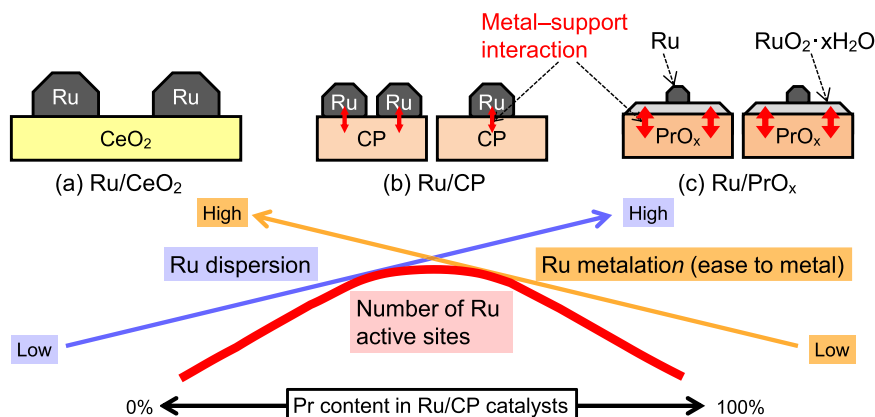

Fig. 14. Mechanism of high activity of Ru/CP catalysts.

Table 1
Comparison of catalytic activity of various catalysts for NH_3 decomposition.

| Catalyst	Ru loading (wt%)	Temperature (°C)	GHSV (mL/g_{cat}·h)	NH_3 decomposition rate (mmol/g_{cat}·s)	TOF_{NH3} (s^{-1})	E_a (kJ/mol)	Reference
Ru/CeO_2–PrO_x	3.0	450	1300,000	1.45	9.4	88.8	This study
Ru/CeO_2–PrO_x	3.0	400	538,000	0.48	3.1	88.8	This study
Ru/CeO_2	3.0	450	1010,000	1.00	9.0	87.6	This study
Ru/PrO_x	3.0	450	1050,000	1.20	11.3	85.7	This study
Ru/CeO_2	2.0	450	138,000	0.15	2.4		[47]
Ru/CeO_2	1.0	450	228,000	1.10			[48]
$Ru/La_{0.33}Ce_{0.67}O_x$	1.8	450	30,000	0.29	7.6	80	[49]
Ru/La_2O_3	4.8	450	18,000	0.16	8.3	34.7	[51]
$Cs_2O/Ru/Pr_6O_{11}$	0.5	350	–	0.03	0.27		[52]
Ru/Pr_2O_3	5.0	450	100,000	0.23	1.4	61.9	[53]
Ru/Sm_2O_3	3.8	450	30,000	0.29	3.6	85.1	[54]
$Ru/BaAl_{12}O_{19}$	2.7	450	60,000	0.15	2.6	65.0	[69]
Cs–Ru–Ba–ZrO_2	3.0	450	30,000	0.14		64.2	[70]
K–Ru/MgO	3.5	450	36,000	0.44			[48]
Ru/MgO	5.0	450	30,000	0.30		74.6	[30]
K–Ru/MgO	5.0	450	36,000	0.39		65.9	[28]
$Ru/CNTs$	5.0	450	150,000	0.16	0.33	69.9	[8]
$RuK/CNTs$	4.8	450	60,000	0.63	1.34	54.5	[21]
K–Ru/MgO–$CNTs$	4.85	400	60,000	0.59			[23]
Ru/MgO	3.0	400	–	0.29	8.5	76.1	[19]

demonstrate a durability at 570 °C for 80,000 h. Fig. 15 shows the NH_3 conversion rate over endurance time. In Fig. 15 the catalyst is Ru/CP33 (Pr content of 33%) and the endurance temperature is 650 °C. The Ru/CP33 catalyst revealed NH_3 conversions over 99.5% under an SV of 30,000 h^{-1} and 500 °C even after 1800 h of use. It should be noted that NH_3 conversion decreased almost linearly with endurance time, and the similar behavior was also observed in our previous study with an Ru/MgO catalyst [13]. The intercept (X_0) and the slope (k) could be obtained from the approximate straight line, and these were regarded as the initial NH_3 conversion and the deterioration rate, respectively. The linear relationship between NH_3 conversion and endurance time indicated that the NH_3 conversion is an extrapolatable parameter to estimate the endurance time. In case the Ru/CP33 catalyst was used in the NH_3 decomposition reactor at an endurance temperature of 650 °C, the endurance time required to maintain NH_3 conversion over 99.5% was expected to be 28,000 h.

In our previous study, the Ru/MgO catalyst used at endurance temperatures of 570 °C and 650 °C, the required endurance times to keep NH_3 conversion over 99.5% were 61,000 h and 6800 h, respectively. At an endurance temperature of 650 °C, the Ru/CP33 catalyst exhibited approximately four times longer endurance time than the Ru/MgO catalyst did. If the Ru/CP33 catalyst maintained the same proportional advantage compared to the Ru/MgO catalyst at the endurance temperature of 570 °C, the endurance time required to maintain NH_3 conversion over 99.5% of the Ru/CP33 catalyst was estimated to be 250,000 h. Therefore, it was concluded that the Ru/CP33 catalyst had sufficient durability as well as sufficient NH_3 decomposition activity for commercialization.

4. Conclusion

Based on a target cost of H_2 production for commercialization, we set the target performance for the NH_3 decomposition catalyst at an on-site H_2 fueling station. The catalyst was required to exceed NH_3 conversion of 99.5% (residual NH_3 concentration < 2500 ppm) at a reaction temperature of 500 °C and a high space velocity (SV) of 30,000 h^{-1} after pretreatment at 550 °C. To increase the SV, we examined CeO_2 and PrO_x as supports, because their bulk densities exceed those of conventional high performance supports.

Ru/CeO_2–PrO_x catalysts with Pr content between 33% and 67%, prepared by a coprecipitation method, achieved the target performance and exhibited the highest level of NH_3 decomposition activity among the catalysts reported in the literature thus far. The effect of Pr in the Ru/CP
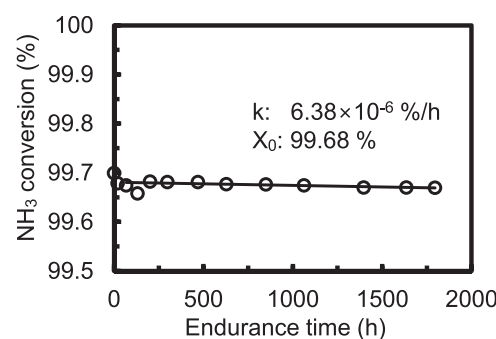
Fig. 15. NH_3 conversion at 500 °C and an SV of 30,000 h^{-1} as a function of endurance time when the endurance temperature is 650 °C.

catalysts prepared by the coprecipitation method was revealed by STEM and in situ XAFS analyses for the first time. The results revealed that Pr enhanced Ru dispersion but also inhibited Ru metalation. Because of these contradictory effects, there is an optimum Pr content between 33% and 67%, which maximizes the number of Ru active sites and the NH_3 decomposition activity. Finally, we confirmed sufficient durability of the Ru/CP catalyst under practical conditions in a microchannel heat-exchanger reactors at on-site H_2 fueling stations.

CRediT authorship contribution statement

Kiyoshi Yamazaki: Conceptualization, Methodology, Formal analysis, Investigation, Writing - Original Draft, Visualization. **Mitsuru Matsumoto:** Investigation, Writing - Review & Editing. **Marie Ishikawa:** Conceptualization, Supervision. **Akinori Sato:** Supervision, Project administration, Funding acquisition.

Declaration of Competing Interest

The authors declare that they have no known competing financial interests or personal relationships that could have appeared to influence the work reported in this paper.

Data availability

No data was used for the research described in the article.

Acknowledgements

Appendix A. Supporting information

Supplementary data associated with this article can be found in the online version at doi:10.1016/j.apcatb.2022.122352.

References

[1] S.A. Sherif, F. Barbir, T.N. Veziroglu, Wind energy and the hydrogen economy – review of the technology, Sol. Energy 78 (2005) 647–660, https://doi.org/10.1016/j.solener.2005.01.002.

[2] M. Balat, Potential importance of hydrogen as a future solution to environmental and transportation problems, Int. J. Hydr. Energy 33 (2008) 4013–4029, https://doi.org/10.1016/j.ijhydene.2008.05.047.

[3] O.V. Marchenko, S.V. Solomin, The future energy: hydrogen versus electricity, Int. J. Hydrog. Energy 40 (2015) 3801–3805, https://doi.org/10.1016/j.ijhydene.2015.01.132.

[4] A. Hasan, I. Dincer, Development of an integrated wind and PV system for ammonia and power production for a sustainable community, J. Clean. Product. 231 (2019) 1515–1525, https://doi.org/10.1016/j.jclepro.2019.05.110.

[5] A. Yapicioglu, I. Dincer, A review on clean ammonia as a potential fuel for power generators, Renew. Sustain. Energy Rev. 103 (2019) 96–108, https://doi.org/10.1016/j.rser.2018.12.023.

[6] Y. Kojima, Hydrogen storage materials for hydrogen and energy carriers, Int. J. Hydr. Energy 44 (2019) 18179–18192, https://doi.org/10.1016/j.ijhydene.2019.05.119.

[7] T.V. Choudhary, C. Sivadinarayana, D.W. Goodman, Catalytic ammonia decomposition: CO_x-free hydrogen production for fuel cell applications, Catal. Lett. 72 (2001) 197–201, https://doi.org/10.1023/A:1009023825549.

[8] S.F. Yin, Q.H. Zhang, B.Q. Xu, W.X. Zhu, C.F. Ng, C.T. Au, Investigation on the catalysis of CO_x-free hydrogen generation from ammonia, J. Catal. 224 (2004) 384–396, https://doi.org/10.1016/j.jcat.2004.03.008.

[9] J. Sakamoto, H. Misono, J. Nakayama, N. Kasai, T. Shibutani, A. Miyake, Evaluation of safety measures of a hydrogen fueling station using physical modeling, Sustainability 10 (2018) 3846–3861, https://doi.org/10.3390/su10113846.

[10] R. Nasharuddin, M. Zhu, Z. Zhang, D. Zhang, A technoeconomic analysis of centralised and distributed processes of ammonia dissociation to hydrogen for fuel cell vehicle applications, Int. J. Hydr. Energy 44 (2019) 14445–14455, https://doi.org/10.1016/j.ijhydene.2019.03.274.

[11] L. Lin, Y. Tian, W. Su, Y. Luo, C. Chen, L. Jiang, Techno-economic analysis and comprehensive optimization of an on-site hydrogen refuelling station system using ammonia: hybrid hydrogen purification with both high H_2 purity and high recovery, Sustain. Energy Fuels 4 (2020) 3006–3017, https://doi.org/10.1039/C9SE01111K.

[12] H. Kubo, Cross-ministerial strategic innovation promotion program (SIP), Energy Carriers. Basic Technology for Hydrogen Station Utilizing Ammonia. ⟨https://www.jst.go.jp/sip/dl/k04/end/team4–5.pdf⟩ (Japanese), (accessed: Sep 30, 2022), 2018, Japan science and technology agency (JST).

[13] K. Yamazaki, M. Matsumoto, H. Kubo, T. Fujitani, M. Ishikawa, A. Sato, Evaluation of durability performance of a Ru/MgO catalyst for ammonia decomposition at an on-site hydrogen fueling station, Ind. Eng. Chem. Res. 61 (2022) 5778–5785, https://doi.org/10.1021/acs.iecr.2c00565.

[14] S. Chiuta, D.G. Bessarabov, Design and operation of an ammonia-fueled microchannel reactor for autothermal hydrogen production, Catal. Today 310 (2018) 187–194, https://doi.org/10.1016/j.cattod.2017.05.018.

[15] N. Engelbrecht, S. Chiuta, D.G. Bessarabov, A highly efficient autothermal microchannel reactor for ammonia decomposition: analysis of hydrogen production in transient and steady-state regimes, J. Power Sources 386 (2018) 47–55, https://doi.org/10.1016/j.jpowsour.2018.03.043.

[16] K. Schumacher, N. Engelbrecht, R.C. Everson, M. Friedl, D.G. Bessarabov, Steady-state and transient modelling of a microchannel reactor for coupled ammonia decomposition and oxidation, Int. J. Hydr. Energy 44 (2019) 6415–6426, https://doi.org/10.1016/j.ijhydene.2019.01.132.

[17] ISO 14687–2. ⟨https://www.iso.org/standard/55083.html⟩ (accessed Sep 30, 2022).

[18] M. Tanimura, T. Nakazawa, On the corrosion embrittlement of commercial steels caused by hydrogen attack and nitriding attack in an ammonia converter, Corros. Eng. Dig. 21 (1972) 209–218, https://doi.org/10.3323/jcorr1954.21.5_209, accessed Sep 30, 2022.

[19] T. Fujitani, I. Nakamura, Y. Hashiguchi, S. Kanazawa, A. Takahashi, Effect of catalyst preparation method on ammonia decomposition reaction over Ru/MgO catalyst, Bull. Chem. Soc. Jpn 93 (2020) 1186–1192, https://doi.org/10.1246/bcsj.20200103.

[20] S.F. Yin, B.Q. Xu, C.F. Ng, C.T. Au, Nano Ru/CNTs: a highly active and stable catalyst for the generation of CO_x-free hydrogen in ammonia decomposition, Appl. Catal. B 48 (2004) 237–241, https://doi.org/10.1016/j.apcatb.2003.10.013.

[21] S.J. Wang, S.F. Yin, L. Li, B.Q. Xu, C.F. Ng, C.T. Au, Investigation on modification of Ru/CNTs catalyst for the generation of CO_x-free hydrogen from ammonia, Appl. Catal. B 52 (2004) 287–299, https://doi.org/10.1016/j.apcatb.2004.05.002.

[22] S.F. Yin, B.Q. Xu, X.P. Zhou, C.T. Au, A mini-review on ammonia decomposition catalysts for on-site generation of hydrogen for fuel cell applications, Appl. Catal. A 277 (2004) 1–9, https://doi.org/10.1016/j.apcata.2004.09.020.

[23] S.F. Yin, B.Q. Xu, S.J. Wang, C.F. Ng, C.T. Au, Magnesia–carbon nanotubes (MgO–CNTs) nanocomposite: novel support of Ru catalyst for the generation of CO_x-free hydrogen from ammonia, Catal. Lett. 96 (2004) 113–116, https://doi.org/10.1023/B:CATL.0000030107.64702.74.

[24] J.C. Ganley, F.S. Thomas, E.G. Seebauer, R.I. Masel, A priori catalytic activity correlations: the difficult case of hydrogen production from ammonia, Catal. Lett. 96 (2004) 177-122.

[25] J. Zhang, H. Xu, Q. Ge, W. Li, Highly efficient Ru/MgO catalysts for NH_3 decomposition: synthesis, characterization and promoter effect, Catal. Commun. 7 (2006) 148–152, https://doi.org/10.1016/j.catcom.2005.10.002.

[26] F. Hayashi, Y. Toda, Y. Kanie, M. Kitano, Y. Inoue, T. Yokoyama, M. Hara, H. Hosono, Ammonia decomposition by ruthenium nanoparticles loaded on inorganic electride C12A7:e⁻, Chem. Sci. 4 (2013) 3124–3130, https://doi.org/10.1039/c3sc50794g.

[27] A. Takahashi, T. Fujitani, Kinetic analysis of decomposition of ammonia over nickel and ruthenium catalysts, J. Chem. Eng. Jpn. 49 (2016) 22–28, https://doi.org/10.1252/jcej.14we431.

[28] X. Ju, L. Liu, P. Yu, J. Guo, X. Zhang, T. He, G. Wu, P. Chen, Mesoporous Ru/MgO prepared by a deposition–precipitation method as highly active catalyst for producing CO_x-free hydrogen from ammonia decomposition, Appl. Catal. B 211 (2017) 167–175, https://doi.org/10.1016/j.apcatb.2017.04.043.

[29] L. Huo, B. Liu, H. Li, B. Cao, X. Hu, X. Fu, C. Jia, J. Zhang, Component synergy and armor protection induced superior catalytic activity and stability of ultrathin Co-Fe spinel nanosheets confined in mesoporous silica shells for ammonia decomposition reaction, Appl. Catal. B 253 (2019) 121, https://doi.org/10.1016/j.apcatb.2019.04.053.

[30] X. Ju, L. Liu, X. Zhang, J. Feng, T. He, P. Chen, Highly efficient Ru/MgO catalyst with surface-enriched basic sites for production of hydrogen from ammonia decomposition, ChemCatChem 11 (2019) 4161–4170, https://doi.org/10.1002/cctc.201900306.

[31] K.G. Kirste, K. McAulay, T.E. Bell, D. Stoian, S. Laassiri, A. Daisley, J.S. J. Hargreaves, K. Mathisen, L. Torrente-Murciano, COx-free hydrogen production from ammonia – mimicking the activity of Ru catalysts with unsupported Co-Re alloys, Appl. Catal. B 280 (2021), 119405, https://doi.org/10.1016/j.apcatb.2020.119405.

[32] J. Cha, T. Lee, Y.J. Lee, H. Jeong, Y.S. Jo, Y. Kim, S.W. Nam, J. Han, K.B. Lee, C. W. Yoon, H. Sohn, Highly monodisperse sub-nanometer and nanometer Ru particles confined in alkali-exchanged zeolite Y for ammonia decomposition, Appl. Catal. B 283 (2021), 119627, https://doi.org/10.1016/j.apcatb.2020.119627.

[33] L. Huo, X. Han, L. Zhang, B. Liu, R. Gao, B. Cao, W.W. Wang, C.J. Jia, K. Liu, J. Liu, J. Zhang, Spatial confinement and electron transfer moderating Mo–N bond strength for superior ammonia decomposition catalysis, Appl. Catal. B 294 (2021), 120254, https://doi.org/10.1016/j.apcatb.2021.120254.

[34] C. Zhou, K. Wu, H. Huang, C.F. Cao, Y. Luo, C.Q. Chen, L. Lin, C. Au, L. Jiang, Spatial confinement of electron-rich Ni nanoparticles for efficient ammonia decomposition to hydrogen production, ACS Catal. 11 (2021) 10345–10350, https://doi.org/10.1021/acscatal.1c02420.

[35] K. Ogasawara, T. Nakao, K. Kishida, T.N. Ye, Y. Lu, H. Abe, Y. Niwa, M. Sasase, M. Kitano, H. Hosono, Ammonia decomposition over CaNH-supported Ni catalysts via an NH^{2-}-vacancy-mediated Mars−van Krevelen mechanism, ACS Catal. 11 (2021) 11005–11015, https://doi.org/10.1021/acscatal.1c01934.

[36] I. Lucentini, X. Garcia, X. Vendrell, J. Llorca, Review of the decomposition of ammonia to generate hydrogen, Ind. Eng. Chem. Res. 60 (2021) 18560–18611, https://doi.org/10.1021/acs.iecr.1c00843.

[37] J. Feng, X. Zhang, J. Wang, X. Ju, L. Liu, P. Chen, Applications of rare earth oxides in catalytic ammonia synthesis and decomposition, Catal. Sci. Technol. 11 (2021) 6330–6343, https://doi.org/10.1039/d1cy01156a.

[38] C. Chen, K. Wu, H. Ren, C. Zhou, Y. Luo, L. Lin, C. Au, L. Jiang, Ru-based catalysts for ammonia decomposition: A mini-review, Energy Fuels 35 (2021) 11693–11706, https://doi.org/10.1021/acs.energyfuels.1c01261.

[39] Y. Gu, Y. Ma, Z. Long, S. Zhao, Y. Wang, W. Zhang, One-pot synthesis of supported Ni@Al₂O₃ catalysts with uniform small-sized Ni for hydrogen generation via ammonia decomposition, Int. J. Hydr. Energy 46 (2021) 4045–4054, https://doi.org/10.1016/j.ijhydene.2020.11.003.

[40] L. Deng, H. Lin, X. Liu, J. Xu, Z. Zhou, M. Xu, Nickel nanoparticles derived from the direct thermal reduction of Ni-containing Ca–Al layered double hydroxides for hydrogen generation via ammonia decomposition, Int. J. Hydr. Energy 46 (2021) 38351–38362, https://doi.org/10.1016/j.ijhydene.2021.09.071.

[41] Q.C. Do, Y. Kim, T.A. Le, G.J. Kim, J.R. Kim, T.W. Kim, Y.J. Lee, H.J. Chae, Facile one-pot synthesis of Ni-based catalysts by cation-anion double hydrolysis method as highly active Ru-free catalysts for green H_2 production via NH_3 decomposition, Appl. Catal. B 307 (2022), 161167, https://doi.org/10.1016/j.apcatb.2022.121167.

[42] H. Fang, D. Liu, Y. Luo, Y. Zhou, S. Liang, X. Wang, B. Lin, L. Jiang, Challenges and opportunities of Ru-based catalysts toward the synthesis and utilization of ammonia, ACS Catal. 12 (2022) 3938–3954, https://doi.org/10.1021/acscatal.2c00090.

[43] Y. Qiu, E. Fu, F. Gong, R. Xiao, Catalyst support effect on ammonia decomposition over Ni/MgAl$_2$O$_4$ towards hydrogen production, Int. J. Hydr. Energy 47 (2022) 5044–5052, https://doi.org/10.1016/j.ijhydene.2021.11.117.

[44] G. Li, H. Zhang, X. Yu, Z. Lei, F. Yin, X. He, Highly efficient Co/NC catalyst derived from ZIF-67 for hydrogen generation through ammonia decomposition, Int. J. Hydr. Energy 47 (2022) 12882–12892, https://doi.org/10.1016/j.ijhydene.2022.02.046.

[45] I. Nakamura, H. Kubo, T. Fujitani, Critical role of Cs doping in the structure and NH$_3$ decomposition performance of Ru/MgO catalysts, Appl. Catal. A 644 (2022), 118806, https://doi.org/10.1016/j.apcata.2022.118806.

[46] Z. Hu, J. Mahin, S. Datta, T.E. Bell, L. Torrente-Murciano, Ru-based catalysts for H$_2$ production from ammonia: effect of 1D support, Top. Catal. 62 (2019) 1169–1177, https://doi.org/10.1007/s11244-018-1058-3.

[47] I. Lucentini, A. Casanovas, J. Llorca, Catalytic ammonia decomposition for hydrogen production on Ni, Ru and Ni−Ru supported on CeO$_2$, Int. J. Hydrog. Energy 44 (2019) 12693–12707, https://doi.org/10.1016/j.ijhydene.2019.01.154.

[48] X.C. Hu, X.P. Fu, W.W. Wang, X. Wang, K. Wu, R. Si, C. Ma, C.J. Jia, C.H. Yan, Ceria-supported ruthenium clusters transforming from isolated single atoms for hydrogen production via decomposition of ammonia, Appl. Catal. B 268 (2020), 118424, https://doi.org/10.1016/j.apcatb.2019.118424.

[49] T.A. Le, Y. Kim, H.W. Kim, S.U. Lee, J.R. Kim, T.W. Kim, Y.J. Lee, H.J. Chae, Ru-supported lanthania–ceria composite as an efficient catalyst for CO$_x$-free H$_2$ production from ammonia decomposition, Appl. Catal. B 285 (2021), 119831, https://doi.org/10.1016/j.apcatb.2020.119831.

[50] I. Lucentini, G.G. Colli, C.D. Luzi, I. Serrano, O.M. Martínez, J. Llorca, Catalytic ammonia decomposition over Ni-Ru supported on CeO$_2$ for hydrogen production: Effect of metal loading and kinetic analysis, Appl. Catal. B 286 (2021), 119896, https://doi.org/10.1016/j.apcatb.2021.119896.

[51] C. Huang, Y. Yu, J. Yang, Y. Yan, D. Wang, F. Hu, X. Wang, R. Zhang, G. Feng, Ru/La$_2$O$_3$ catalyst for ammonia decomposition to hydrogen, Appl. Surf. Sci. 476 (2019) 928–936, https://doi.org/10.1016/j.apsusc.2019.01.112.

[52] K. Nagaoka, T. Eboshi, N. Abe, S. Miyahara, K. Honda, K. Sato, Influence of basic dopants on the activity of Ru/Pr$_6$O$_{11}$ for hydrogen production by ammonia decomposition, Int. J. Hydr. Energy 39 (2014) 20731–20735, https://doi.org/10.1016/j.ijhydene.2014.07.142.

[53] X. Zhang, L. Liu, J. Feng, X. Ju, J. Wang, T. He, P. Chen, Ru nanoparticles on Pr$_2$O$_3$ as an efficient catalyst for hydrogen production from ammonia decomposition, Catal. Lett. 150 (2022) 1170–1181, https://doi.org/10.1007/s10562-021-03709-2.

[54] X. Zhang, L. Liu, J. Feng, X. Ju, J. Wang, T. He, P. Chen, Metal–support interaction-modulated catalytic activity of Ru nanoparticles on Sm$_2$O$_3$ for efficient ammonia decomposition, Catal. Sci. Technol. 11 (2021) 2915–2923, https://doi.org/10.1039/d1cy00080b.

[55] T. Nonaka, K. Dohmae, Y. Hayashi, T. Araki, S. Yamaguchi, Y. Nagai, Y. Hirose, T. Tanaka, H. Kitamura, T. Uruga, H. Yamazaki, H. Yumoto, H. Ohashi, S. Goto, Toyota beamline (BL33XU) at SPring-8, AIP Conf. Proc. 1741 (2016), 030043, https://doi.org/10.1063/1.4952866.

[56] Y. Nagai, K. Dohmae, K. Teramura, T. Tanaka, G. Guilera, K. Kato, M. Nomura, H. Shinjoh, S. Matsumoto, Dynamic in situ observation of automotive catalysts for emission control using X-ray absorption fine structure, Catal. Today 145 (2009) 279–287, https://doi.org/10.1016/j.cattod.2008.10.031.

[57] R.D. Shannon, Revised effective ionic radii and systematic studies of interatomic distances in halides and chalcogenides, Acta Cryst. A 32 (1976) 751–767, https://doi.org/10.1107/S0567739476001551.

[58] I. Arčon, A. Benčan, A. Kodre, M. Kosec, X-ray absorption spectroscopy analysis of Ru in La$_2$FeRuO$_5$, X-Ray Spectrom. 36 (2007) 301–304, https://doi.org/10.1002/xrs.946.

[59] W. Zheng, J. Zhang, H. Xu, W. Li, NH$_3$ decomposition kinetics on supported Ru clusters: Morphology and particle size effect, Catal. Lett. 119 (2007) 311–318, https://doi.org/10.1007/s10562-007-9237-z.

[60] A.M. Karim, V. Prasad, G. Mpourmpakis, W.W. Lonergan, A.I. Frenkel, J.G. Chen, D.G. Vlachos, Correlating particle size and shape of supported Ru/γ-Al$_2$O$_3$ catalysts with NH$_3$ decomposition activity, J. Am. Chem. Soc. 131 (2009) 12230–12239, https://doi.org/10.1021/ja902587k.

[61] D. Xuezhi, Z. Jinghong, Q. Gang, L. Ping, Z. Xinggui, C. De, Carbon nanofiber-supported Ru catalysts for hydrogen evolution by ammonia decomposition, Chin. J. Catal. 31 (2010) 979–986, https://doi.org/10.1016/S1872-2067(10)60097-6.

[62] Y. Nagai, T. Hirabayashi, K. Dohmae, N. Takagi, T. Minami, H. Shinjoh, S. Matsumoto, Sintering inhibition mechanism of platinum supported on ceria-based oxide and Pt-oxide–support interaction, J. Catal. 242 (2006) 103–109, https://doi.org/10.1016/j.jcat.2006.06.002.

[63] R.T. Sanderson, Chemical Periodicity, Reinhold Pub. Corp.,, New York, 1960.

[64] G. Yang, G. Yu, X. Huang, F. Peng, H. Wang, Effect of calcium dopant on catalysis of Ir/La$_2$O$_3$ for hydrogen production by oxidative steam reforming of glycerol, Appl. Catal. B 127 (2012) 89–98, https://doi.org/10.1016/j.apcatb.2012.08.003.

[65] Z.J. Wan, Y.K. Tao, H.Z. You, X. Zhang, J. Shao, Na-ZSM-5 Zeolite Nanocrystals Supported Nickel Nanoparticles for Efficient Hydrogen Production from Ammonia Decomposition, ChemCatChem 13 (2021) 3027–3036, https://doi.org/10.1002/cctc.202100324.

[66] N. Jeon, S. Kim, A. Tayal, J. Oh, W. Yoon, W.B. Kim, Y. Yun, Y-doped BaCeO$_3$ perovskite-supported Ru catalysts for CO$_x$-free hydrogen production from ammonia: Effect of strong metal−support interactions, ACS Sustain. Chem. Eng. 10 (2022) 15564–15573, https://doi.org/10.1021/acssuschemeng.2c04995.

[67] A. Suda, K. Yamamura, Y. Ukyo, T. Sasaki, H. Sobukawa, T. Tanabe, Y. Nagai, M. Sugiura, Effect of specific surface area of ceria-zirconia solid solutions on their oxygen storage capacity, J. Ceram. Soc. Jpn. 112 (2004) 581–585, https://doi.org/10.2109/jcersj.112.581.

[68] M. Kikugawa, Y. Goto, K. Kobayashi, T. Nanba, H. Matsumoto, H. Imagawa, Efficient ammonia synthesis over Ru/CeO$_2$–PrO$_x$ catalysts with controlled Ru dispersion by Ru-Pr interaction, J. Catal. 413 (2022) 934–942, https://doi.org/10.1016/j.jcat.2022.08.004.

[69] Z. Wang, Z. Cai, Z. Wei, Highly active ruthenium catalyst supported on barium hexaaluminate for ammonia decomposition to CO$_x$ free hydrogen, ACS Sustain. Chem. Eng. 7 (2019) 8226–8235, https://doi.org/10.1021/acssuschemeng.8b06308.

[70] Z. Wang, Y. Qu, X. Shen, Z. Cai, Ruthenium catalyst supported on Ba modified ZrO$_2$ for ammonia decomposition to CO$_x$-free hydrogen, Int. J. Hydr. Energy 44 (2019) 7300–7307, https://doi.org/10.1016/j.ijhydene.2019.01.235.